SANDIA REPORT
SAND2002–2063
Unlimited Release
Printed July 2002

Salt Mechanics Primer for Near-Salt and Sub-Salt Deepwater Gulf of Mexico Field Developments

A. F. Fossum and J. T. Fredrich

Prepared by
Sandia National Laboratories
Albuquerque, New Mexico 87185 and Livermore, California 94550

Sandia is a multiprogram laboratory operated by Sandia Corporation, a Lockheed Martin Company, for the United States Department of Energy under Contract DE-AC04-94AL85000.

Issued by Sandia National Laboratories, operated for the United States Department of Energy by Sandia Corporation.

Available to DOE and DOE contractors from
Office of Scientific and Technical Information
P.O. Box 62
Oak Ridge, TN 37831

Prices available from (615) 576-8401, FTS 626-8401

Available to the public from
National Technical Information Service
U.S. Department of Commerce
5285 Port Royal Rd
Springfield, VA 22161

NTIS price codes
Printed copy: A03
Microfiche copy: A01

SAND2002-2063
Unlimited Release
Printed July 2002

Salt Mechanics Primer for Near-Salt and Sub-Salt Deepwater Gulf of Mexico Field Developments

A. F. Fossum and J. T. Fredrich
Geoscience and Environment Center
Sandia National Laboratories
P.O. Box 5800
Albuquerque, NM 87185-0750

Abstract

The Gulf of Mexico (GoM) is the most active deepwater region in the world and provides some of the greatest challenges in scope and opportunity for the oil and gas industry. The complex geologic settings and significant water and reservoir depths necessitate high development costs, in addition to requiring innovating technology. The investment costs are substantial: because of the extreme water depths (up to 8000 feet) and considerable reservoir depths (to 30,000 feet below mudline), the cost of drilling a single well can be upwards of 50 to 100 million dollars. Central, therefore, to successful economic exploitation are developments with a minimum number of wells combined with a well service lifetime of twenty to thirty years. Many of the wells that are planned for the most significant developments will penetrate thick salt formations, and the combined drilling costs for these fields are estimated in the tens of billions of dollars. In May 2001, Sandia National Laboratories initiated a Joint Industry Project focused on the identification, quantification, and mitigation of potential well integrity issues associated with sub-salt and near-salt deepwater GoM reservoirs. The project is jointly funded by the DOE (Natural Gas and Oil Technology Partnership) and nine oil companies (BHP Billiton Petroleum, BP, ChevronTexaco, Conoco, ExxonMobil, Halliburton, Kerr-McGee, Phillips Petroleum, and Shell). This report provides an assessment of the state of the art of salt mechanics, and identifies potential well integrity issues relevant to deepwater GoM field developments. Salt deformation is discussed and a deformation mechanism map is provided for salt. A bounding steady-state strain rate contour map is constructed for deepwater GoM field developments, and the critical issue of constraint in the subsurface, and resultant necessity for numerical analyses is discussed.

This page intentionally left blank.

Table of Contents

This page intentionally left blank.

List of Figures

This page intentionally left blank.

List of Tables

This page intentionally left blank.

1 Background

The deepwater Gulf of Mexico (GoM) is the most active deepwater region in the world and currently provides some of the greatest challenges in scope and opportunity for the industry (*Oil & Gas J.*, May 1 & June 26, 2000). The deepwater GoM is estimated to contain undiscovered recoverable resources of at least ~13 billion boe, and is known to harbor some exceptional reservoirs such as the recent Thunder Horse discovery at water depth over 6,000 feet with estimated recoverable reserves of at least 1 billion boe *(AAPG Explorer*, Sept. 1999). However, the complex salt tectonics and extreme water and reservoir depths necessitate very high development costs, in addition to requiring innovating technology to bring these fields on stream (*Oil & Gas J.*, May 1, 2000).

The investment costs associated with these deepwater GoM fields are substantial. Because of the extreme water depths (up to 8000 feet) and considerable reservoir depths (to 30,000 feet below mudline), the cost of drilling a single well can be upwards of 50 to 100 million dollars. Central, therefore, to the successful economic exploitation are field developments with a minimum number of wells combined with a well service lifetime of twenty to thirty years. Many of the wells that are planned for the most significant developments will penetrate thick salt formations, and the combined drilling costs for these wells are estimated in the tens of billions of dollars.

In May 2001, Sandia National Laboratories initiated a Joint Industry Project focused on the identification, quantification, and mitigation of potential well integrity issues associated with sub-salt and near-salt deepwater GoM reservoirs. The project is jointly funded by the DOE under its Natural Gas and Oil Technology Partnership and nine oil and gas companies (BHP, BP, ChevronTexaco, Conoco, ExxonMobil, Halliburton, Kerr-McGee, Phillips Petroleum, and Shell). The intent of this report is to provide an assessment of the state of the art of salt mechanics, and to identify, based on the existing knowledge base, potential well integrity issues relevant to deepwater GoM field developments.

2 A Primer on Salt Mechanics

2.1 Deformation behavior of salt

Polycrystalline salt exhibits deformation behavior that is similar to the deformation behavior of rocks in the brittle regime and of metals in the ductile regime. It creeps under any deviatoric stress. For a given mean stress, it takes less shear stress to deform salt in pure shear than it does in either triaxial compression or triaxial extension. For mean normal stresses typically less than about 5 MPa (725 psi) it will dilate with time upon application of a deviatoric stress, but it will flow with constant volume above a mean stress of ~5 MPa (725 psi). The brittle failure of salt, defined as the shear stress at peak load, is pressure sensitive and a function of plastic strain. It is stronger in triaxial compression than in triaxial extension. The strain rate of salt is a strong function of temperature, and increases with increasing temperature.

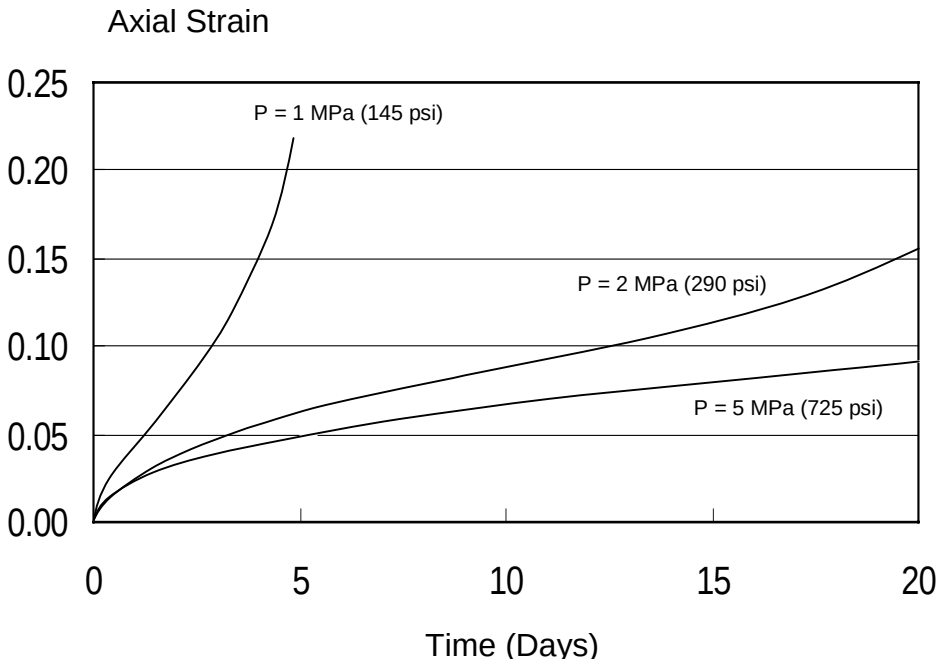

Figure 2.1. Creep behavior of polycrystalline salt at 25 °C and a stress difference of 25 MPa for confining pressures of 1, 2, and 5 MPa.

The creep of salt involves either two or three creep stages. For confining pressures typically less than 5 MPa (725 psi), salt specimens subjected to a constant stress state will pass through three stages. In the first stage, called primary creep, the strain rate begins with a very high rate and decreases to a constant rate. The time during which the specimen deforms at constant rate is called the secondary creep stage. The third stage is called tertiary creep in which the strain rate increases until failure occurs. For confining pressures typically above 5 MPa (725 psi) only the primary and secondary regimes are evident. Figure 2.1 illustrates the creep behavior of salt at three different levels of confining pressure. The strain-time curves for confining pressures higher than 5 MPa (725 psi) are identical to the one conducted at 5 MPa (725 psi). Therefore, creep results obtained under a confining pressure of at least 5 MPa (725 psi) are expected to be appropriate for deepwater GoM conditions for which the mean stresses are extremely high.

2.2 Deformation mechanism map for salt

To develop the structural prediction technology to model the complex behavior of natural salt occurring at the Waste Isolation Pilot Plant (WIPP) site, Sandia National Laboratories embarked upon a long-term program in the late 1970's that included extensive laboratory testing, constitutive model development, and field testing for validation. It was decided at the outset that to develop the requisite predictive capability commensurate with the needs of the U.S. defense programs in a regulatory context, it would be desirable to rely on first principles or, where that was impossible, on laboratory empirical data as the proper basis for the technology. To this end, a deformation mechanism map for natural salt was constructed for use in developing steady-state creep constitutive equations. This map is

illustrated in Figure 2.2 and discussed in detail in Appendices A and B. The hashed portion on the map shows where the expected conditions lay for deepwater GoM field developments. This region encompasses three deformation mechanisms, dislocation glide at very high shear stresses, dislocation climb for high temperatures, and a well characterized but undefined mechanism(s) for lower shear stresses and temperatures.

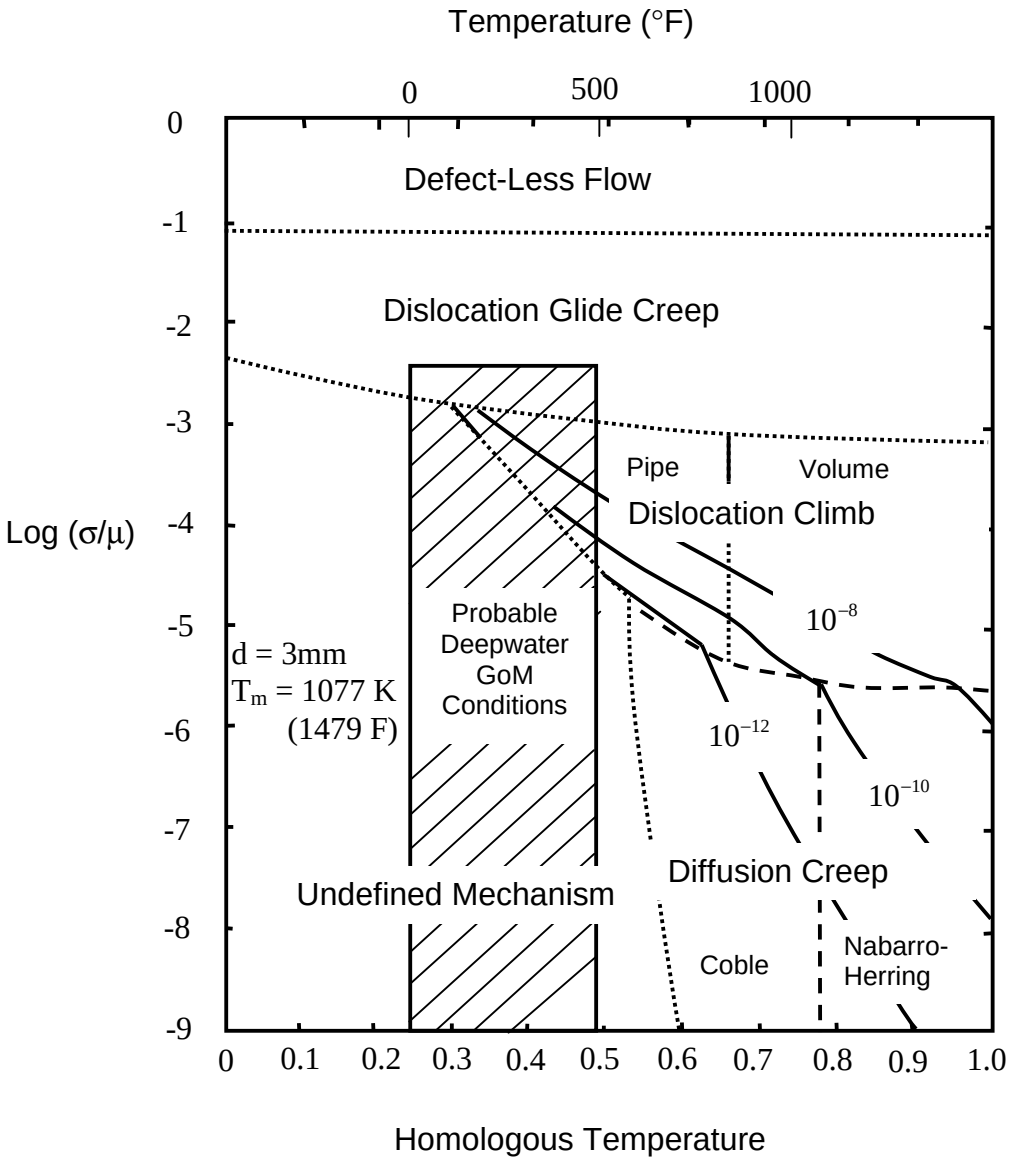

Figure 2.2. Deformation mechanism map for salt showing the location of probable deepwater GoM conditions. Consistent with standard practices, temperature as indicated in the abscissa is normalized by the melting temperature of the solid (equal to 1479 °F for salt) to yield homologous temperature. Likewise, the stress difference σ (equal to twice the maximum shear stress) as indicated in the ordinate is normalized by the shear modulus μ.

2.3 Sandia MDCF salt model

The constitutive model developed at Sandia for WIPP analyses is called the Multimechanism Deformation Coupled Fracture (MDCF) model. This model has been formulated by considering individual deformation and fracture mechanisms that include dislocation creep, shear damage, tensile damage, and damage healing. This model, which is implemented in Sandia's finite element codes, is described in detail later in this report.

The MDCF model is significant because it is based, as much as possible, on first principles (i.e., identified deformation and fracture mechanisms), as opposed to a phenomenological model that is based on macroscopic observations. This aspect is important because the former approach is required to extrapolate beyond the conditions used in the laboratory to determine the constitutive parameters for the model. While a phenomenological model may fit experimental data very well, it is not necessarily a good predictor for conditions of pressure, temperature, and time outside of the laboratory experiments.

2.4 Laboratory testing of salt and parameter evaluation

Salt creep is characterized by three important types of behavior that must be handled appropriately when material model parameters are evaluated in the laboratory. These aspects are damage, transient strain, and steady-state creep rate. Some of the steady-state creep parameters are determined theoretically, based on identified deformation mechanisms, as discussed previously. The remaining parameters must be determined experimentally from macroscopic laboratory measurements. Generally, the steady-state creep parameters are evaluated first, followed by the transient creep parameters and then the damage parameters. The tests used most often to evaluate the parameters are confined triaxial compression creep tests in which a solid right circular cylinder of salt is loaded hydrostatically to a prescribed pressure level followed by additional axial load to induce a deviatoric stress in the specimen. Specimen deformations are then measured with time while the confining pressure, deviatoric stress, and temperature are held constant.

The reason the steady-state creep parameters are determined first is that the damage and transient creep rates can be eliminated such that the steady-state parameters can be determined independently of the other parameters. The damage is eliminated by using a sufficiently high confining pressure. The transient creep rate is eliminated by allowing the creep test to run long enough to let the transient behavior die out leaving only steady-state deformation. Once the steady-state parameters have been evaluated they are held fixed and the transient parameters are determined by fitting the material model to the transient part of the creep tests. Finally the transient and steady-state creep parameters are held fixed and the damage parameters are determined by fitting the material model to creep tests conducted at very low confining pressures.

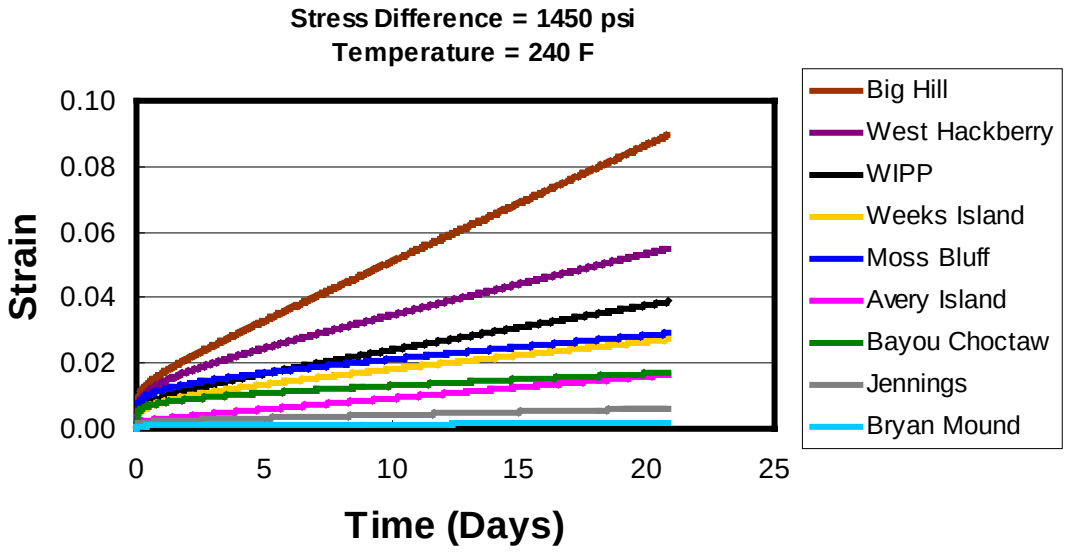

Figure 2.3. Comparison of creep behavior (to 21 days) for WIPP and Gulf Coast domal salts.

2.4.1 Salt ranking

A very large database exists for WIPP salt because this salt has been studied and characterized perhaps more than any other salt in the world (see Appendix C). While there are fewer data for U.S. Gulf Coast salt domes, the material parameters for the Sandia creep model have been evaluated for many of these domes. It is possible therefore to compare the behavior of the U.S. Gulf Coast salt domes with WIPP salt. As illustrated in Figure 2.3, the creep deformation of WIPP salt falls in the middle of the range of deformations exhibited by the gulf coast domes. Because so much is known about WIPP salt and because it appears to represent nominal gulf coast salt dome behavior, it is convenient to use WIPP salt as a baseline salt and to assign as "strong" and "weak" those salts that exhibit lower and higher creep rates than WIPP salt, respectively.

2.4.2 A deepwater Gulf of Mexico salt – Mad Dog

A preliminary creep test was conducted at TerraTek, Inc. on Mad Dog Salt Sample #3 (9478.9ft) with a confining pressure of 1,000 psi, a stress difference of 2,000 psi and a temperature of 220 °F. Figure 2.4 shows that the measured strain rate is very similar to that predicted for the Bayou Choctaw salt using the same conditions. Thus, it appears that the Mad Dog salt can be classified as a "strong" salt according to the definition given above.

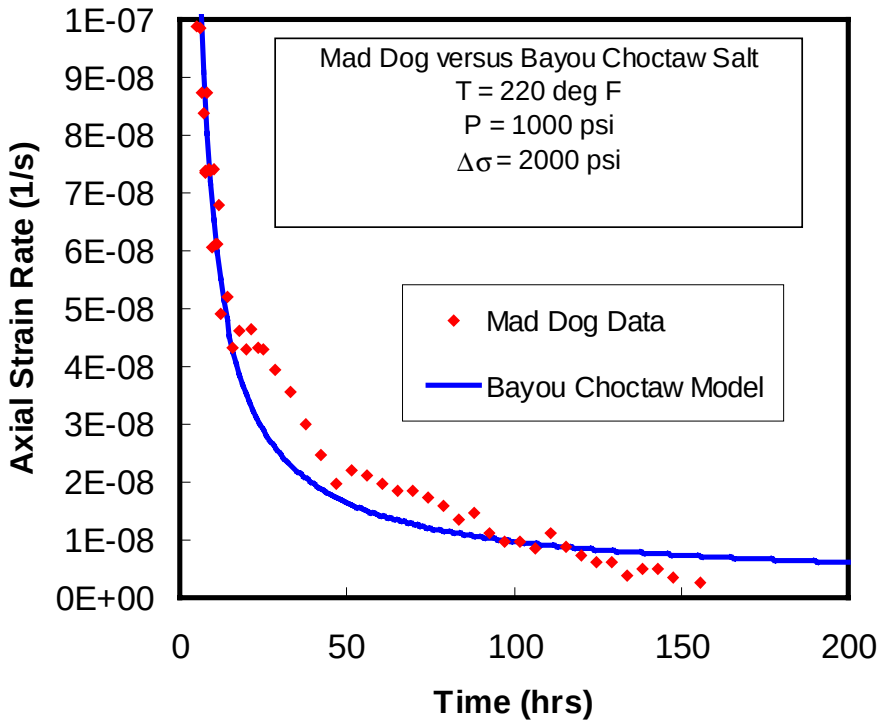

Figure 2.4. Comparison of axial strain rates predicted with the Sandia salt model using Bayou Choctaw salt properties and the measured results from Mad Dog Salt Sample #3.

2.5 Controls on salt creep

It is well known that the strength and deformation properties of salt are site dependent. There is some evidence to suggest that such variability is caused by differences in salt chemistry, mineralogy, or other physical characteristics such as subgrain size, grain size distribution, or grain aspect ratio. For example, *Hansen et al*. (1987) demonstrated that increases in anhydrite content reduce creep rates. In 1995 the Solution Mining Research Institute (SMRI) commissioned RE/SPEC Inc. to compile a database of strength and deformation properties and chemical, mineralogic and physical characteristics of U.S. Gulf Coast domal salts from RE/SPEC's government-funded and industry-funded characterization studies.

The database assembled experimental data on salt recovered from 12 domes located along the U.S. Gulf and was evaluated to determine correlations amongst strength and deformation properties and chemical, mineralogic, and physical characteristics of dome salt. The analyses are described in Appendix D, and the findings are summarized below.

- Subgrain size is a good indicator of strength and deformation properties for U.S. Gulf Coast dome salt. Steady-state strain rate and the steady-state stress exponent are inversely correlated with subgrain size, with correlation coefficients (ρ) of -0.87 and -0.92, respectively.

- The steady-state strain rate determined at a temperature of 373 K and a stress difference of 5 MPa is correlated with mean grain size (ρ = 0.96) and with grain aspect ratio (ρ = 0.89).
- For impure salts, at 373 K the steady-state stress exponent shows a direct correlation with both sodium and chlorine (~0.90). Similar correlations for this exponent were found for halite (0.92) an anhydrite (-0.92).
- For impure salts, the steady-state stress exponent shows strong correlation with sodium (ρ = 0.9), chlorine (ρ = 0.9), calcium (ρ = -0.9), and sulfate (ρ = -0.9).
- For impure salts, the steady-state strain rate determined at a temperature of 298 K and a stress difference of 20.69 MPa is correlated with magnesium (ρ = 0.77).
- For impure salts, the angle of internal friction is correlated with potassium (ρ = 0.7) and with water insolubles (ρ = 0.77), while cohesion is inversely correlated with water insolubles (ρ = -0.77).
- Steady-state strain rates and the steady-state stress exponents are directly correlated with strength parameters, while the thermal activation energy parameters are inversely correlated with strength parameters.
- An inverse correlation exists between cohesion and the angle of internal friction (-0.64).
- Direct correlation was found for tensile strength and unconfined compressive strength (0.74), tensile strength and cohesion (0.66), and unconfined compressive strength and cohesion (0.79).

2.6 Bounding steady-state strain rate contour map for salt for deepwater GoM conditions in the absence of geometrical and structural constraints

It is shown in Section 2.4.1 that WIPP salt, although from a bedded formation, can be considered representative of the known deformation behaviors of U.S. Gulf Coast salt domes. Thus, assuming that U.S. Gulf Coast salt domes are representative of deepwater GoM salt domes, sheets, rafts, and pillars, it is useful to use the extensive knowledge of WIPP salt to make predictions of behavior for deepwater GoM conditions. Figure 2.5 shows the steady-state strain rates calculated for WIPP salt using the MCDF constitutive model described in Appendix E for the range of shear stresses and temperatures represented by the hashed portion of the deformation mechanism map depicted in Figure 2.2.

Also shown in Figure 2.5 are stress profiles as a function of depth from the mudline (nominal 4000 ft water depth) associated with most likely (shale) and worst (sand) case scenarios defined as follows. A generic overburden profile was used to calculate the vertical stress profile for normally pressured formations. Two relationships were then used to compute the magnitude of the minimum horizontal stress. The first (most likely) is based on an empirical relationship used to compute minimum horizontal stresses in shales in the Gulf of Mexico. The second profile (worst case) is computed for sands that have a lower Poisson's ratio than the shale, and so have a lower minimum horizontal stress. For both profiles, the stress difference used for the calculations shown in Figure 2.5 is the overburden stress minus the minimum horizontal stress. The in-situ temperatures follow the relationship of 38 °F at mudline, and a temperature gradient increase of 1.45 °F per 100 ft depth.

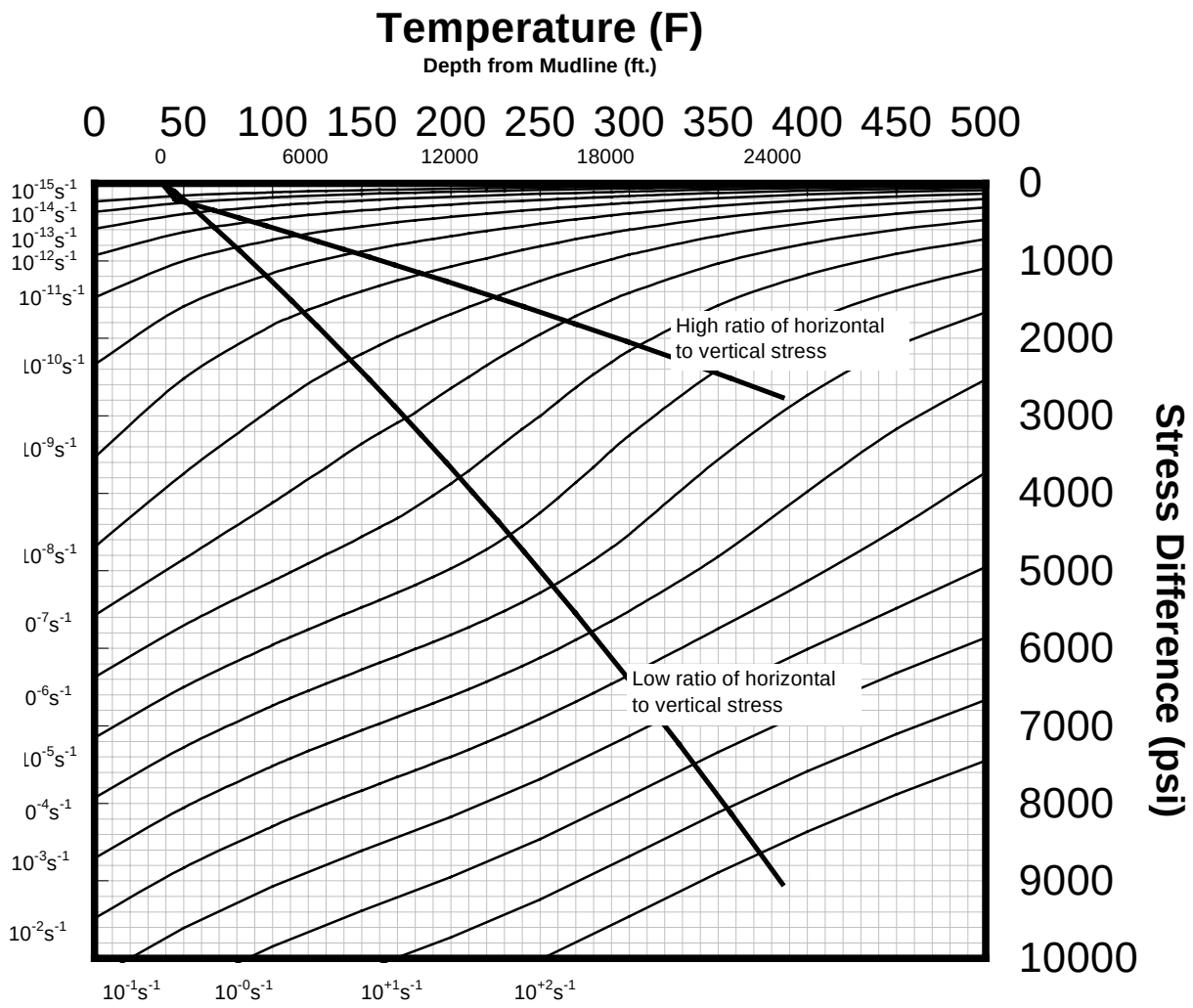

Figure 2.5. Contour map of steady-state strain rates for salt in expected conditions for deepwater GoM field developments, in the absence of geometrical and structural constraints. The two lines bound the expected stress and temperature conditions.

2.7 Comments on the applicability of the salt strain–rate contour map for deepwater GoM field developments

2.7.1 The issue of constraint in the field setting of interest

It is critical to recognize that the strain rates shown in Figure 2.5 are creep rates. The significance of this is that the creep rates correspond to fixed or constant stresses. Since stress is a function only of the elastic strain (i.e., not the inelastic or total strain), this implies that the elastic strain rates are zero. However, this is not the case in the subsurface where the stresses in the region of interest are affected by the constraint imposed by the overburden, sideburden, and underburden formations.

In a laboratory creep test, a specimen is loaded to a certain stress level and then the stresses are held constant while the specimen is allowed to deform with time. Except for the elastic load-up strain, all subsequent strain is inelastic, and since the elastic strain is zero, this also represents the total strain. Thus, the creep test represents a structural problem that is 'statically determinate', meaning that the stresses can be determined from equilibrium equations alone. However, this is generally not the case in the subsurface; instead the full set of equilibrium equations, compatibility equations, and constitutive equations must be solved simultaneously with the necessary initial and boundary conditions. This is a much more complicated problem than the simple laboratory test, and accurate prediction of the deformation rates in a real field setting requires application of numerical methods such as the finite element method. Only with numerical methods can one simultaneously solve the equilibrium equations, compatibility equations, and constitutive equations subject to the imposed initial and boundary conditions.

If a salt body in the subsurface is suddenly subjected to a significant stress difference, this stress difference will produce an instantaneous inelastic strain rate. Without transient effects, this inelastic strain rate will equal the strain rate corresponding to the stress difference as shown in Figure 2.5. In the subsurface, however, the salt will be constrained and the elastic strain rate will not be zero. The total strain rate will be the sum of the elastic strain rate and the inelastic strain rate. Because of constraint, the total strain rate may be small or even close to zero. If the inelastic strain rate were high but the total strain rate were constrained to be small, then the elastic strain rate would have the opposite sign of the inelastic strain rate such that the sum of the elastic and inelastic strain rates equals the total strain rate. *This process results in a stress change.* So, while very high stress differences in the subsurface may produce very high inelastic strain rates in the salt, the in situ stresses will likely change very rapidly as well. The only way to determine what the total strain rate is in the salt, and thus how much the salt moves, is to solve the complete set of equilibrium, compatibility, and constitutive equations with the appropriate initial and boundary conditions.

2.7.2 The stress state at the interface between salt and non-salt formations

Because of the requirement for the salt body to be in equilibrium and to maintain continuity with the surrounding formations, the stress state at the interface with the salt body may be highly complex and variable. Consider the simple case of a spherical salt body that is surrounded by a non-salt geologic formation with three different principal stresses. The stresses in the salt will relax and ultimately reach a hydrostatic stress state, as long as the far field stresses are not perturbed, and as long as the surrounding formation is constrained. But because of the stress relaxation in the salt body, the stress state in the non-salt formation immediately surrounding the salt will be different from the far field stress state to maintain equilibrium and continuity. For example, the principal stresses may rotate, or equivalently, shear stresses will appear in the horizontal and vertical planes. This is illustrated for the simple case of a spherical salt body in Figure 2.6. These stress rotations may have implications for the long-term integrity of well casings at the interface between salt and non-salt formations.

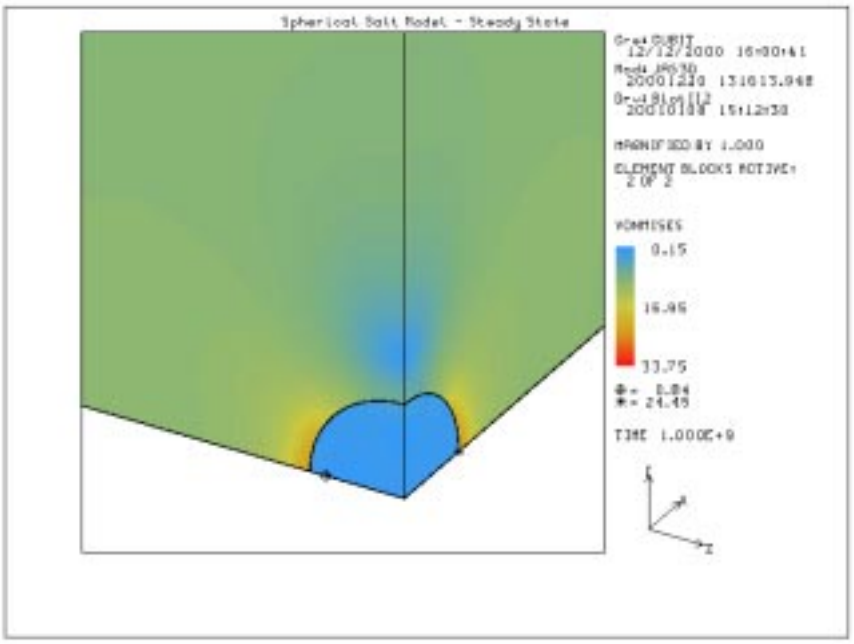

Figure 2.6. Contours of von Mises stress around a spherical salt body that is constrained in a uniform overburden with unequal vertical and horizontal stresses. The stress differences in the salt body approach zero because of the inability of the salt to maintain deviatoric stresses. Consequently, the stress state in the near-field takes up the load that the salt sheds, i.e., the near-field stresses are perturbed from the far-field conditions as required to satisfy the equilibrium conditions. The stress difference in the far-field is as defined by the initial in situ stress state applied.

2.7.3 Possible effects of production-induced temperature changes

Temperature changes may propagate into the overburden formations over the field lifetime from the heated fluids that are produced up the wellbore from greater depths. These temperature changes will have two independent influences. Firstly, thermal stresses will be induced by the thermal loading. In particular, these thermally induced stresses will include shear stresses that may be the most critical at the interface between different formations, i.e. at the interface between the salt body and overburden formation. The second effect of the anticipated temperature changes is that the creep behavior of the salt body will change in two ways. The steady state creep behavior will change since creep is accomplished by thermally activated deformation mechanisms. In addition, the thermal loads will also result in transient strain due to the stress perturbation. None of these potential factors are considered in Figure 2.5.

2.7.4 The issue of transient strain

Another complicating factor is transient strain. Whenever there is a stress change or perturbation, salt instantaneously responds by straining at a much higher or lower value than

the steady-state value depending on whether the stress change results in increased or decreased loading, respectively. In general, whenever there is a perturbation in the stress field, transient strain is significant. In the Sandia salt model, a transient function modifies the multi-mechanism steady-state strain rate to accommodate changing strain rates associated with changes in the stress fields, such as would be the case during excavation, drawdown, or heating or cooling.

For deepwater GoM applications, transient strain processes may or may not be important. During drilling (excavation) and production (pore pressure drawdown), stresses in the subsurface will change, causing transient creep. The strain contributions due to transient creep are expected to be significant for a time period on the order of tens of days. The question of whether or not these transient strains may impact either wellbore stability during drilling or long-term well integrity over the field lifetime depends upon the magnitude of the stress perturbations that are experienced. Experience to date suggests that wellbore stability problems during drilling typically result from difficulties in predicting pore pressure fracture gradients below the salt body. Further, these difficulties are experienced less often in the deepwater where the sediment layer is thinner than along the shelf (*Bevan et al.*, 1999). In regard to long-term well integrity issues, as discussed above, it is not possible to predict *a priori* the magnitude of the stress perturbations that will be experienced during production without numerical modeling.

2.8 The necessity for numerical analyses

Back of the envelope calculations for subsurface structural engineering situations involving salt and other materials are generally not possible even for purely steady-state considerations. This is because salt is highly nonlinear and because the scenarios of interest are, for the most part, structural problems that are statically indeterminate. This means that the complete set of governing equations must be solved as required in any well-posed problem. This requires knowledge not only of the creep behavior of salt but also of its elastic properties and thermal properties. In addition, the solution of practical problems involving salt requires an understanding of the loading and history of loading, i.e., the initial state of the salt, along with the other requisite elements of a structural boundary value problem.

2.9 Summary of some basic facts about salt

Some of the issues relating to salt structural mechanics for the ranges of temperature and stress that will be experienced in deepwater GoM field developments are summarized below and discussed in more detail in Appendices A and B.

1. Elastic and thermal properties of salt do not vary significantly from site to site.
2. Inelastic behavior and failure of salt can vary significantly from site to site.
3. For the range of temperatures that will be experienced in deepwater GoM field developments, the specific heat and density can be considered constant.
4. Salt is a very good conductor of heat.

5. The thermal conductivity can be represented as a nonlinear function of temperature.
6. The coefficient of linear thermal expansion can be represented as a quadratic function of temperature.
7. The shear modulus is a linear function of temperature and Poisson's ratio is constant.
8. The elastic behavior can be considered linear.
9. Increasing the temperature at a given stress greatly increases the inelastic deformation rate of salt.
10. Nearly all inelastic dilatancy in salt is suppressed above a mean stress of 5 MPa.
11. Salt will deform inelastically under any nonzero stress difference.
12. It takes less shear stress to deform salt in pure shear than it does in triaxial compression or in triaxial extension.
13. The transient inelastic deformation of salt is extremely rate sensitive and the rate is a non-linear function of stress, temperature, and history of deformation.
14. The steady-state creep rate of salt depends only on stress and temperature.
15. Significant increases in deformation rate of polycrystalline salt are observed with increase in moisture content when substantial microcracking and dilatancy occur at low confining pressures. This is not expected for the range of stresses anticipated for deepwater GoM field developments.
16. The failure of salt in shear depends nonlinearly on mean stress.
17. It is easier to fail salt in triaxial extension than in triaxial compression for low mean stresses but not for high mean stresses.
18. Small changes in shear stress cause very large changes in time-to-failure but an order-of-magnitude increase in loading rate produces only a modest increase in strength.
19. Once damaged through stress-induced microcracking, salt will heal itself under pressure.
20. The transient deformation of salt is extremely important whenever there is a perturbation in the stress field such as that resulting from excavation or thermal loading.
21. Although the conditions expected for deepwater GoM field development are more severe than those encountered in the WIPP or SPR programs, they nonetheless fall within the ranges of stress and temperature for which mechanistically based salt models have been developed and tested.
22. Although from bedded origin, WIPP salt is typical of Gulf Coast dome salts falling nearly in the middle of the deformation behavior of SPR dome salts.
23. Subgrain size is a good indicator of strength and deformation properties for dome salt.
24. Steady-state strain rate is weakly correlated with mean grain size and grain aspect ratio.
25. High correlations have been observed for the interdependence of strength and deformation properties with chemical, and mineralogic characteristics.

3 Appendix A – Laboratory Observations of Salt Deformation Behavior

The thermo-mechanical behavior of salt is divided into the following four categories: thermal behavior, elastic deformation, inelastic deformation, and failure. A comparison of data from different sites shows that thermal and elastic behavior do not vary significantly from site to site (*Yang*, 1981, *Hansen et al*., 1984; *Krieg*, 1984), but that inelastic behavior and failure vary significantly among different sites. These laboratory observations include the ranges of stress, temperature, and deformation rates of interest for production from deepwater sub-salt and near-salt GoM reservoirs.

The extent to which each of the four above categories contributes to observed behavior depends on temperature, stress, and the history of deformation. The following sections address the influences of temperature, stress, time (rate), and history on deformation. Mechanical behavior is also influenced by moisture. However, except for moisture effects on inelastic deformation, little data are available to make an assessment of the importance of moisture on other categories of behavior.

3.1 Thermal behavior

3.1.1 Thermal conductivity, specific heat, and density

Only thermal conductivity varies significantly with temperature for the range of temperatures that will be experienced by salt in deepwater GoM field developments. The specific heat and density can be considered constant and equal to 862.8 J/kg-K and 2163 Kg/m^3, respectively. The thermal conductivity can be represented as a function of temperature as (*Krieg*, 1984)

$$\lambda = 5.40\left(\frac{300}{T}\right)^{1.14} \tag{3.1}$$

where T is in degrees kelvin. This expression for thermal conductivity has been compared to data for salt from Germany where it was found that the values compared to within $\pm 3\%$ from room temperature to 200 ˚C (392 ˚F).

3.1.2 Thermal expansion

When salt at constant load is heated it expands. This thermal expansion is described by the coefficient of linear thermal expansion. Mathematically this expansion is expressed by

$$\alpha = \frac{1}{L}\left(\frac{\partial L}{\partial T}\right)_{\sigma} \tag{3.2}$$

where α is the coefficient of linear thermal expansion, L is the length over which the expansion is measured and $(\partial L / \partial T)_{\sigma}$ is the partial derivative of length with respect to temperature at constant stress. Thus, the coefficient of linear thermal expansion gives the change in unit length per unit change in temperature at constant stress.

3.1.3 Temperature effects

Yang (1981) has summarized the measurement of the coefficient of linear thermal expansion of salt over a wide range of temperatures. For the range of temperatures applicable to deepwater GoM field developments, the temperature dependence of the coefficient of linear thermal expansion is given by

$$\alpha = 3.025x10^{-5} + 2.942x10^{-8}T - 2.5677x10^{-12}T^2 \tag{3.3}$$

where T is in degrees Kelvin and α has units K^{-1}. Over a temperature range of 25 ˚C (298 K, 77 ˚F) to 250 ˚C (523 K, 482 ˚F) the value of the coefficient of linear thermal expansion varies from 38.8 x 10^{-6} to 44.9 x 10^{-6}, which represents a 15% increase.

3.1.4 Stress effects

For pressures between 3 MPa (435 psi) and 25 MPa (3625 psi) over a temperature range of 35 ˚C (95 ˚F) to 210 ˚C (410 ˚F), *Durham et al*. (1987) have shown no discernible influence of pressure on the thermal expansion of salt.

3.2 Elastic deformation

Elastic deformation is reversible. That is, upon removal of stresses a body returns to its original unstressed dimensions. The elastic deformation of salt is assumed, because of a lack of data to the contrary, to be linear and isotropic. This means that there is no orientation effect and the elastic deformation is described by Hooke's Law containing two elastic constants. Hooke's Law is given by

$$\varepsilon_{ij}^{e} = \frac{1}{E}\left[(1+\upsilon)\sigma_{ij} - \upsilon\sigma_{kk}\delta_{ij}\right] \tag{3.4}$$

where ε_{ij}^{e} are the components of the elastic strain tensor; σ_{ij} are the components of the stress tensor; E is Young's modulus; and υ is Poisson's ratio. These elastic constants appear to be site independent as can be seen in Table 3.1.

Table 3.1. Room temperature elastic constants for natural rock salts (*Hansen et al.,* 1984).

Site	Young's Modulus (GPa)			Poisson's Ratio		
	Mean	σ [b]	Range	Mean	σ [b]	Range
WIPP	NA[a]	NA[a]	29.6-36.5	NA[a]	NA[a]	0.17-0.26
Permian	26.6	3.7	19.0-33.4	0.33	0.05	0.24-0.41
Paradox	31.0	3.4	25.2-36.3	0.36	0.10	0.09-0.50
Jefferson Island	29.5	3.5	25.0-34.4	0.29	0.07	0.17-0.39
Week's Island	30.5	7.1	21.5-42.3	NA[a]	NA[a]	NA[a]
Cote Blanche	24.1			0.41		
Avery Island	30.6	5.8	21.0-38.2	0.38	0.06	0.31-0.47
Richton	31.5	3.0	26.7-36.4	0.36	0.09	0.21-0.55
Vacherie	31.1	3.5	27.6-37.6	0.34	0.03	0.29-0.39

[a]Not available
[b]Standard deviation

3.2.1 Temperature effects

From the small number of studies that have been performed to study the influence of temperature on the elastic constants of salt it can be concluded that the stiffness of salt decreases as temperature increases. *Frost and Ashby* (1982) found the change in shear modulus *G* to be given by

$$\frac{dG}{dT} = -0.01 GPa / K \tag{3.5}$$

while *Pfeifle et al*. (1983) found no temperature dependence for Poisson's ratio, ν, for the range of temperatures applicable to deepwater GoM field developments. Since Young's modulus, *E*, is expressible in terms of the shear modulus and Poisson's ratio, the change in *E* with temperature, according to Eq. 3.4, would be given by

$$\frac{dE}{dT} = -0.02 \times (1.0 + \upsilon) GPa / K \tag{3.6}$$

3.2.2 Stress effects

Although some pressure effects have been reported, they are not consistent. When the elastic constants are determined from unload-reload stress-strain curves it appears that the elastic constants are stress independent, and furthermore, linear for the entire unload-reload cycles. Therefore, the linear elastic assumption is appropriate for salt in the elastic regime.

3.2.3 History effects

Based on the work of *Pfeifle et al*. (1983) there is no apparent dependence of the elastic constants on the strain (or stress) at which the unload-reload cycle is performed. It is thus reasonable to conclude that the values of the elastic constants for salt are independent of history.

3.3 Inelastic deformation

The discussion in this section is qualitative because there is no generally accepted model for the inelastic behavior of salt. Thus, sensitivity to temperature, stress, etc. for specific constants will not be assessed. When salt is loaded and then unloaded, some permanent deformation is always observed. This inelastic deformation is caused by the motion of line imperfections in the crystal, called dislocations, mass diffusion, and, at sufficiently low pressures, microcracking.

3.3.1 Temperature effects

Increasing the temperature at a given stress greatly increases the inelastic deformation of salt. This fact has been documented by numerous investigators who have found that the temperature dependence of inelastic deformation is highly nonlinear. The deformation becomes more ductile as temperature increases and crystalline plasticity dominates intercrystalline microcracking.

3.3.2 Stress effects

Mean stress (pressure) up to about 5 MPa (725 psi) influences inelastic deformation (*Chan et al.*, 1994). Above a mean stress of 5 MPa nearly all inelastic deformation in the form of dilatancy is suppressed. Shear stress strongly influences inelastic deformation and the dependence is strongly nonlinear. Some constitutive modelers assume that the shear stress dependence is a power function with a stress exponent ranging from 2 to 9. Still others assume that the dependence is an exponential or hyperbolic sine, with the hyperbolic sine being used for high values of shear stress.

There appears to be no threshold value of shear stress below which salt does not deform inelastically. For example in a stress relaxation test performed at room temperature (*Senseny et al*., 1992), the stress at the end of the test was 0.25 MPa (36.25 psi) and still decreasing. In a stress relaxation test the stress will decay to a threshold value and then remain constant. For salt, this value appears to be zero.

Some investigators have found that salt creep is influenced by the type of stress state (*Munson and Fossum*, 1986, *Munson et al.*, 1990). For example, it takes less shear stress to deform salt in pure shear than it does in triaxial compression or in triaxial extension.

3.3.3 Rate effects

The inelastic deformation of salt is extremely rate sensitive. This is shown clearly by the continued deformation under constant stress in a creep test, the deformation rate dependence of stress in a constant strain rate test, and the stress drop at constant strain in a relaxation test (*Senseny and Fossum*, 1995). The rate dependence is a non-linear function of stress, temperature and deformation.

3.3.4 History effects

Thermomechanical history, in addition to the current stress and temperature, influences the inelastic deformation of salt. However, steady-state creep rate depends only on stress and temperature. Thus, only transient deformation is history dependent.

3.3.5 Moisture effects

Single crystals of salt exhibit a strong moisture effect. For example they show an increase in ductility when deformed in the presence of water, and can sustain large inelastic deformations without fracturing (*Joffe et al*., 1924). The same is not true for fully dense polycrystalline salt since so few crystals are exposed to moisture. However, significant increases in deformation rate are observed with increase in moisture content when substantial microcracking and dilatancy occur such as during a creep test at low confining pressure. At high confining pressure microcracking and dilatancy are suppressed and thus moisture has only a small effect on deformation rate (*Brodsky and Munson*, 1991). On unconfined specimens it has been found (*Varo and Passaris*, 1977) that only the transient creep rate is influenced noticeably by changes in moisture. Steady-state creep is unaltered. This suggests that moisture enhances stress corrosion cracking and accelerates only the brittle mechanism.

Additionally, it has been observed by *Spiers et al*. (1988) that if the inelastic strain rate is less than 10^{-7} s^{-1} the stress required to deform saturated specimens is much less than that required to deform dry specimens. This behavior suggests that there may be a critical strain rate below which moisture effects become significant.

3.4 Brittle failure

We define failure here as the point at which salt begins to lose its load-bearing capacity. In laboratory tests, this corresponds to the peak stress in a constant strain-rate test, or to the onset of tertiary creep in a constant stress test.

3.4.1 Temperature effects

Salt deforms so rapidly with increasing temperature that it is difficult to fail a specimen because the deformations exceed the capacity of the test system. Thus little data exist to show the influence of temperature on salt failure. We do know, however, that increasing the temperature from 20 ˚C (68 ˚F) to 50 ˚C (122 ˚F) does not significantly influence the unconfined compressive strength (*Senseny et al*., 1992). The effect of temperature on the brittle failure of salt is uncertain for the range of temperatures and pressures of interest for deepwater GoM field developments.

3.4.2 Stress effects

The brittle failure of salt is affected significantly by stress. Pressure alone does not produce failure, but it does affect the magnitude of shear stress required to cause failure, including the failure mode and the time required to produce failure. For a constant strain rate, the shear stress required to cause failure increases with pressure. At very high confining pressures (e.g., 50 MPa), excessive specimen deformation prohibits imposition of stresses large enough to cause failure in the laboratory. Also, the magnitude of shear stress required to produce failure at a given mean stress depends on the type of stress state (*Mellegard et al.*, 1992). For example, it takes more shear stress to fail a specimen in a triaxial compression test than it does in a triaxial extension test. Moreover, the ratio of the failure strength in triaxial compression to that in triaxial extension decreases as the pressure increases (*Hunsche*, 1984). At a relatively low confining pressure such as 5 MPa (725 psi) this ratio is between 1.8 and 2.0, but decreases to 1.1 to 1.2 at a pressure of 50 MPa (7,250 psi).

3.4.3 Rate effects

An order-of-magnitude increase in loading rate, at least at 24 ˚C (75.2 ˚F), produces only a modest increase (~10%), in strength (*Hansen and Mellegard*, 1980). In typical laboratory tests in which the strain rates range from $10^{-6} – 10^{-4}$ s^{-1}, there is little influence of rate on shear stress at failure (*Hansen and Mellegard*, 1980).

3.5 Summary

Thermal Behavior. For the expected conditions of sub-salt deepwater GoM field developments, specific heat and density can be considered constant while the thermal conductivity varies significantly with temperature.

Thermal Expansion. Over the temperature range of interest to sub-salt deepwater GoM field developments, the coefficient of linear thermal expansion can be accurately represented by the second-order polynomial as given in Eq. 3.3.

Elastic Deformation. The elasticity of salt may be regarded as linear with temperature-dependent elastic constants.

Inelastic Deformation. Temperature, stress, loading rate, and history strongly influence the inelastic deformation of salt. Moisture also influences the inelastic deformation but is less well-documented. An increase in temperature causes an increase in inelastic deformation. An increase in pressure increases strength and reduces brittle deformation. Inelastic deformation is not a unique function of the current values of stress, temperature and rate but also depends on the history of deformation. The rate of inelastic deformation depends strongly on stress. In particular, higher shear stresses result in higher rates of deformation. It takes less shear stress to deform salt at a given rate in pure shear than it does in triaxial compression or in triaxial extension.

Failure. Salt failure depends on stress and loading rate. Shear stress at failure increases with increasing pressure. At constant pressure, the shear stress at failure is greatest at triaxial compression and decreases as the stress moves towards triaxial extension.

4 Appendix B – Micromechanics

Here, we summarize what is known about salt at the atomistic scale in terms of the basic physical processes governing deformation, hardening and recovery. These processes are called deformation mechanisms and are identified from observable microstructure. Each deformation mechanism has a rate that depends on stress and temperature in a way that characterizes that mechanism. Thus, for any given stress and temperature, a single deformation mechanism usually accounts for most of the observed deformation. A stress-temperature diagram that defines the region in which each deformation mechanism operates is called a deformation mechanism map. These maps have been determined for many crystalline materials, including salt. Fig. 4.1 shows a deformation mechanism map constructed by *Munson* (1979) for salt. Note that the shaded region includes the region of interest for deepwater GoM field developments. In much of this region, there is some uncertainty and debate regarding the identification of a specific deformation mechanism, although the region has been well characterized experimentally. The strain increases as stress and temperature increase and the substructures become better developed. At low stresses, temperatures, and strain levels, the first substructural change is an increase in dislocation density. The increase in dislocation density over the natural density occurs at strains much less than one percent. Dislocations cluster along preferred crystallographic planes at slightly greater strain levels. As strain increases, these diffuse bands evolve into sharp, linear glide bands. As temperature increases result in greater strain, the individual bands become wavy and cross-link. These substructures sometimes appear as elongated polygons and at temperatures above one-third of the melting temperature and strain of a few percent, equant polygons form. At large strain, dynamic recrystallization may be an important mechanism.

The rate-controlling mechanisms are a strong function of temperature. The dominant mechanisms from low temperature to high temperature, or from small strains to large strains are the following:

1. Dislocation Glide
2. Dislocation Cross Slip
3. Diffusional Processes

Mechanisms such as the unknown mechanisms at low temperature and low stress and grain boundary sliding and microcracking are also known to be important. In the following sections the physical description and the substructures will be discussed and related to the phenomenology.

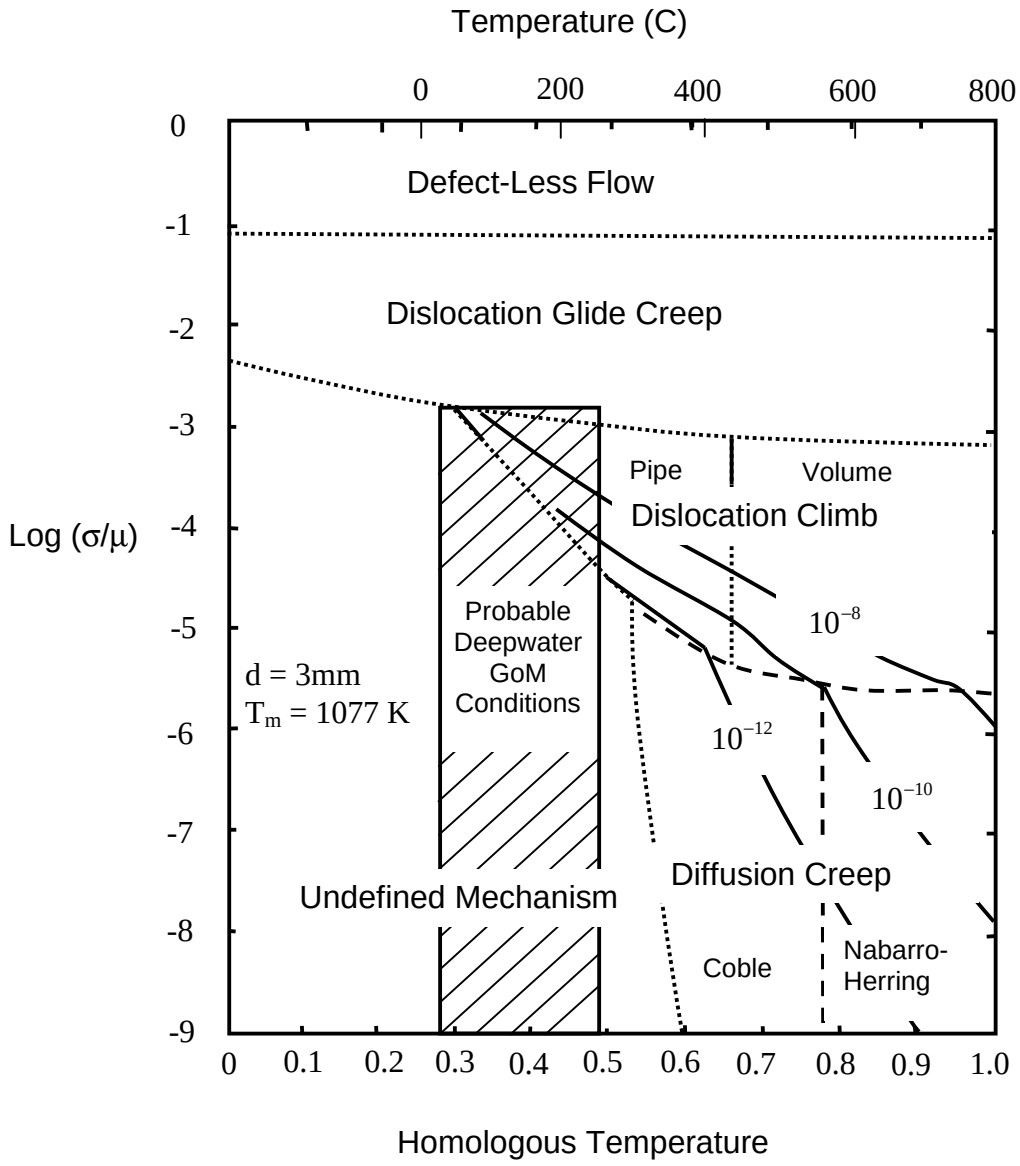

Figure 4.1. Deformation mechanism map for salt.

4.1 Deformation mechanisms and recovery processes

4.1.1 Mechanism 1: Dislocation glide – physical description

For the NaCl structure, plastic deformation by glide results from dislocation motion on a family of crystallographic planes and the easy glide plane is one that does not bring ions of like charge together. This system of six glide planes and directions is denoted as $\{110\}\langle 1\bar{1}0\rangle$. Along a particular plane and direction, the rate of glide increases with the resolved shear stress.

4.1.2 Dislocation glide – microscopic observations

There have been numerous natural salt specimens deformed under the conditions of interest to deepwater GoM field developments that contain glide bands. *Carter and Hansen* (1983) give a comprehensive summary of published observations. The glide bands show as photoelastic effects along {110} in thin chips or sections in cross-polarized light. Also, in etched surfaces of a cleaved chip, the glide bands stand out as linear arrays of pits.

4.1.3 Dislocation glide – phenomenology

Strain hardening phenomena can be caused by dislocation glide. This hardening results from dislocation pile-ups at obstacles such as grain boundaries or by intersection of dislocations. A greater probability for interaction exists as more dislocations are produced. Hardening results when tangles, created by interactions, impede other dislocations. Similarly, dislocations piling up at a grain boundary cause a stress field that impedes subsequent dislocation motion. If no recovery processes are active, the dislocations distort the cubic crystal lattice and produce the photoelastic effects.

4.1.4 Mechanism 2: Dislocation cross slip – physical description

Dynamic recovery relieves the increasing strain energy caused by dislocation pile-ups. The first of the dynamic recovery processes that operate in the NaCl structure is cross-slip (*Skrotzki*, 1982). Cross-slip involves the movement of screw dislocations out of their present plane into any plane that contains the same Burger's vector. This process allows the gliding dislocation to move to another glide plane to avoid an obstacle. Since cross-slip does not require diffusion, it is very important at relatively low temperatures and does not depend strongly on temperature.

4.1.5 Dislocation cross slip – microscopic observations

Photomicrographs of salt strained axially to 0.06 at 15 MPa confining pressure and 75 ˚C show straight, crystallographically controlled bands indicative of glide connected by webs of apparently unorderly arrays of cross-slip systems. Microstructurally, this phenomenon is called wavy slip in which the sharp glide bands indicative of $\{110\}\langle 1\bar{1}0\rangle$ glide are obscured by an undulatory fabric.

4.1.6 Dislocation cross slip – phenomenology

Five independent slip systems are required for homogeneous plastic deformation of a polycrystal with random grain distribution (*von Mises*, 1928). Six crystallographically distinct slip systems of $\{110\}\langle 1\bar{1}0\rangle$ and $\{100\}\langle 1\bar{1}0\rangle$ are available in halides but only two

and three, respectively, are independent (*Skrotzki*, 1983). *Carter and Heard* (1970) showed that under conditions that would be of interest to deepwater GoM field developments the $\{110\}\langle 1\bar{1}0\rangle$ are the only active glide planes. However, other experiments on rock salt have shown a stress-strain-time behavior indicative of general plasticity, that is, the complete absence of fracture, strain hardening and apparent steady-state creep. Cross-slip reconciles this inconsistency.

The onset of cross-slip has been likened to the brittle-to-ductile transition by *Skrotzki and Haasen* (1983). They observed slip lines in various halides and correlated the change in slip behavior on {110} from planar to wavy with the temperature of the brittle-to-ductile transition. Cross-slip then appears to be the primary dynamic recovery mechanism operating at the relatively low temperatures of interest. At the lower temperatures, however, many experiments on natural salt do not involve large strains. At high strain, the continued effectiveness of cross-slip has not been evaluated.

4.1.7 Mechanism 3: Climb-controlled mechanisms

This section discusses glide with climb, whereas the two previous sections discussed glide and glide with cross-slip. Glide with climb is often called just climb because the climb process actually controls the deformation rate even though the plastic deformation results from glide. At elevated temperatures climb is a well-documented recovery mechanism that has been shown to contribute significantly to the deformation. Activation energies of diffusion of the anion and cation of NaCl have been measured in the laboratory. The temperatures at which diffusion completely controls deformation are not likely to be relevant for geoengineering applications.

4.1.8 Climb-controlled mechanisms – physical description

Gliding dislocations eventually encounter obstacles and their mobility is retarded. The process by which the dislocation can move perpendicular to its glide plane is called climb. Atoms are added or removed along the dislocation by diffusion enabling the dislocation to climb. By systematically stacking dislocations, the climb process reduces strain energy in the crystal lattice. Because it depends on the stepwise migration of jogs in the dislocation line, climb is a slow process, much slower than glide. The process is controlled by diffusion of the bulkier anion Cl^-, as it is the slower diffusing ion. Agreement has been demonstrated for metals between the value inferred for activation energy from high-temperature creep experiments and values of activation energy of self-diffusion (*Dorn*, 1956). The similarity is taken as the best evidence that diffusion controls the high-temperature creep rate. However, over the range of interest for salt in geoengineering, the activation energies calculated from creep-test data are not constant. One explanation is that different activation energies indicate a change in rate control between Na^+ and Cl^- diffusion (*Arieli et al.*, 1982). Another explanation is that the mechanisms are changing as a function of temperature or other experimental variables.

4.1.9 Climb-controlled mechanisms – microscopic observations

If sufficient strain accumulates in the specimen, climb-controlled deformation results in substructural polygon arrays. Polygonized salt structures were observed microscopically and discussed in detail by Carter and coworkers (*Carter and Hansen*, 1983, *Carter et al.*, 1982). The subgrain size at steady state is inversely proportional to applied shear stress. It is less clear what the influences of other variables are such as strain rate and temperature. At 200 C when climb is easily thermally activated, a polygonized substructure develops at low strain, less that four percent, and sustains steady state creep strains greater than 0.30.

4.1.10 Climb-controlled mechanisms – phenomenology

At high temperature, diffusion-controlled mechanisms are responsible for steady-state creep. Diffusion is required for climb of dislocations, a recovery process that leads to lower internal strain energy. By relieving the internal strain, climb allows for the continued multiplication and glide of dislocations without an increase in applied shear stress. Climb, as a recovery process, balances the hardening processes and results in steady-state deformation.

4.1.11 DIffusion-controlled mechanisms

Diffusion controlled mechanicsms, i.e. Nabarro-Herring and Coble creep, fall outside of the ranges of stress and temperature that are anticipated for deepwater GoM field developments and are not discussed further.

4.1.12 Dynamic recrystallization

For long-term response, dynamic recrystallization may be an important recovery process. Except at very high temperatures the process has not been well studied in salt. Single crystals were tested by *Guillope and Poirier* (1979) at temperatures between 250 ˚C and 790 ˚C and axial strain levels of more than 0.4. However, recrystalllization has also been discovered in natural salt deformed at the modest temperature of 70 ˚C. Since recrystallization is a recovery process that often results in strain softening, this observation may be very important to understanding long-term deformation of natural salt.

4.1.13 Dynamic recrystallization – physical description

Recrystallization is a dynamic, thermally activated recovery process. Steady-state deformation is a balance between workhardening processes and recovery processes. Dynamic recrystallization occurs when the intracrystalline recovery processes operate too slowly to balance the strain-induced hardening. The process involves grain nucleation and

grain boundry migration into regions of high strain energy. The new grain is initially soft and strain free and proceeds to deform in another sequence of hardening followed by recrystallization.

In deformed crystalline bodies, dynamic recrystallization is an effective way of lowering the strain energy. While it has been studied extensively for many years in metallurgy, it has rarely been observed in natural salt deformed under geoengineering conditions likely because the specimens have undergone insufficient strain.

4.1.14 Dynamic recrystallization – microscopic observations

Photomicrographs of recrystallized substructures are common in the literature. Examples can be found in standard textbooks illustrating cold-worked and annealed microstructures of metals. Dynamic recrystallization at high temperature of single crystals of salt has also been photographed and published (*Guillope and Poirier*, 1979). However, dynamic recrystallization of natural rock salt deformed under conditions of interest to deepwater GoM field developments has only rarely been observed (*Spiers et al.*, 1986).

4.1.15 Dynamic recrystallization – phenomenology

The stress-strain behavior associated with dynamic recrystallization has been documented for many metals and some geologic materials, including halite. Dynamic recrystallization is a softening process, and its occurrence modifies the appearance of the flow curves. Strain softening via recrystallization can result in a stress drop during constant strain rate tests or strain rate increases during constant stress tests.

4.1.16 Summary of mechanisms

At low temperature and small strains, glide is a significant mechanism. Since wavy slip is seen in many specimens deformed between room temperature and 100 ˚C, it may be a very important mechanism. There have been many observations documented on recovery by climb, resulting in polygonized subgrain arrays. However, the associated activation energies inferred from laboratory experiments over the range of temperatures of interest to deepwater GoM field developments are much lower than an activation energy for diffusion of Cl^-. Finally, in salt deformed to high strain, recrystallization has been observed.

4.2 Fracture mechanisms

The fracture mechanisms in natural salt at ambient temperature are cleavage and creep fracture. The failure boundaries of both cleavage and creep fracture have been calculated (*Chan et al.*, 1996). The results are presented in the form of a fracture mechanism map in Figure 4.2, which shows the failure boundaries in the stress space of $-\sigma_1$ and $-\sigma_3$. The

dashed/dotted line represents the stress loci within which constant-volume creep occurs without damage. The solid line represents the cleavage fracture loci at which unstable cleavage fracture occurs. The region between the dashed/dotted line and the solid line depicts stress states where dilatational creep with damage and creep fracture would occur after an unspecified time of creep.

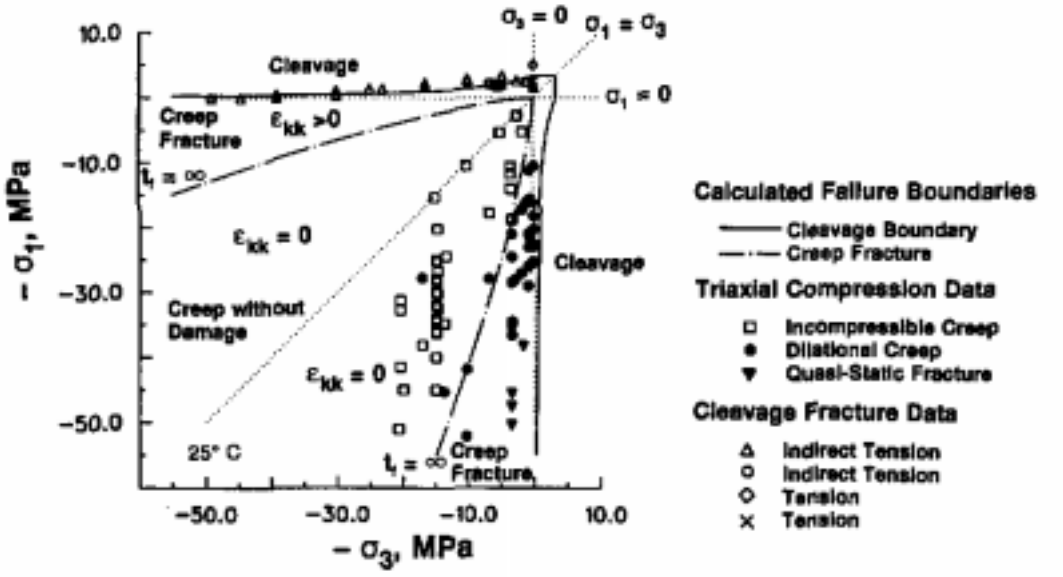

Figure 4.2. Comparison of calculated fracture mechanism map with experimental data for natural salt.

A fracture mechanism map has also been calculated for the stress space of stress difference and confining pressure, and the result is presented in Figure 4.3 (*Chan et al.*, 1996). The calculated fracture mechanism map is in good agreement with experimental data for WIPP salt (*Fossum et al*.,1993; *Van Sambeek et al*., 1993; *Senseny*, 1986; *Wawersik and Hannum*, 1979), and ASSE salt (*Hunsche*, 1993), as shown if Figure 4.3. The cleavage fracture boundaries were calculated using a wing-crack model and the Griffith fracture criterion. The failure boundaries of the creep damage mechanisms are described in terms of isochronous failure curves, which are stress contours of constant creep rupture time. The isochronous failure curve with a failure time of infinity was used to define the boundary between regions where creep occurs with and without damage. Isochronous curves of a time-to-rupture of one hour were used to depict failure regimes where creep crack growth is expected to dominate because of the short failure time. On this basis, the fracture mechanism map in Figure 4.3 is divided into seven failure regimes; (1) Region A, where constant-volume creep occurs without rupture; (2) Region C, where dilatational flow occurs with microcrack damage; (3) Region D, where fracture occurs by wing-crack extension; (4) Region E, where creep failure occurs by a mixture of tensile and shear damage; (5) Region F, where tensile creep crack growth dominates; (6) Region G, where cleavage fracture by wing-crack initiation dominates; and (7) Region H, where cleavage fracture by the Griffith crack dominates.

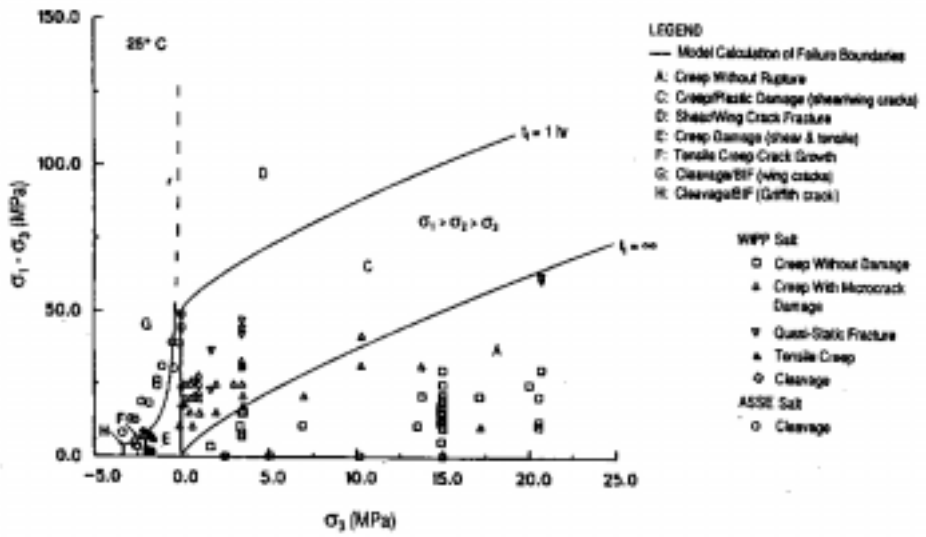

Figure 4.3. Computed fracture mechanism map compared against experimental data of WIPP salt and ASSE salt.

5 Appendix C – Computational Salt Mechanics Experience and Simple Application to Near-Salt and Sub-Salt Deepwater GoM Field Developments

5.1 Waste Isolation Pilot Plant (WIPP)

The WIPP program was established to develop the essential technology for a repository in the bedded salt formations of southeastern New Mexico in response to the need to dispose of the existing nuclear waste products generated by U.S. defense programs. Nearly fifty years ago the National Academy of Sciences recognized that natural salt deposits were desirable host rocks for disposal of radioactive waste. A key advantage of salt deposits for the permanent disposal of such waste is that creep closure of the disposal rooms will eventually encapsulate the waste. These wastes must be isolated from the accessible environment and humankind for 10,000 years. To meet the stringent regulatory requirements for nuclear waste disposal and to assure the public safety, it was necessary to predict the closure times and repository conditions upon encapsulation with much more certainty than is typical of most conventional engineering projects. As a consequence, one of the most important technical challenges of the WIPP Program was to predict accurately the time at which this encapsulation occurs. The development of structural prediction methods was incorporated within a thermal/structural interactions program that was particularly concerned with creep prediction technology. Such prediction technology involves numerical simulations of the response of the complicated excavation geometries of an actual repository and requires technically sophisticated, precise calculations using validated computer codes.

The WIPP program had the benefit of previous work in salt through the Department of Energy's National Waste Terminal Storage (NWTS) program to provide for the safe disposal of commercially-generated nuclear wastes. The goal of the NWTS Program was to locate, design, construct, license, operate, and decommission geologic waste isolation systems in basalt, granite, salt (both bedded and domal), and tuff. Much of the NWTS program work in salt made use of early power-law models of salt. These models were transient models that hardened with strain or time but were not capable of representing with sufficient accuracy the real behavior of salt under complex thermo-mechanical load paths. In the WIPP program, the approach adopted from the onset was to develop the necessary technology based on interpretations of physical and mechanical aspects of the problem and on laboratory generated databases, independent of any assumed or measured underground response. However, this independent technology was to be validated through careful comparison to the extensive collection of in situ data on room closure and salt displacement obtained for that purpose from underground in situ tests at the WIPP facility.

A relatively sophisticated model, that was proposed initially by *Munson and Dawson* (1979), was based on micromechanistic concepts as determined with the use of a deformation mechanism map constructed by *Munson* (1979) for salt. For expected WIPP conditions, three deformation mechanisms needed to be included in the constitutive model. These mechanisms include dislocation glide at higher stress levels, dislocation climb at higher temperatures, and an undefined, but fully characterized empirically, mechanism at

lower temperatures. The overall steady-state creep rate can be considered as the sum of the creep rates of these individual mechanisms acting simultaneously. Transient creep was handled in a limited manner in this initial model.

The first comparison of model predictions with actual in situ data obtained from measurements at the WIPP site showed that the measured room closures and closure rates were at least a factor of three greater than the calculated closures and closure rates. It was demonstrated (*Morgan et al*., 1986) through a parametric study that the discrepancy could not be the result of known uncertainties in steady-state creep parameters or clay seam friction values, but was more deeply rooted.

Munson and Fossum (1986) identified some of the potential sources for the discrepancy. Three major components of the formulation were identified for re-evaluation, (1) the stress generalization, (2) the constitutive kinetic equations, (3) and the values of the material parameters. These investigations resulted in some important discoveries that significantly modified the existing concepts of salt creep and its mathematical representation:

(1) The proper stress generalization for salt creep is not octahedral shear stress leading to the conventional Prandtl-Reuss equations, but rather the maximum principal stress difference, as appears in Tresca plasticity. This conclusion was postulated because dislocation deformation mechanisms respond to the magnitude of the local shear stress. It was borne out experimentally (*Munson et al*., 1990) in thin-walled hollow cylinder creep tests conducted on salt under different types of stress states.
(2) The transient deformation of salt is extremely important whenever there is a perturbation in the stress field. It was found necessary to (*a*) make improvements to the transient strain function by replacing the earlier linear approximation with a quadratic one, (*b*) to make the transient strain limit a function of temperature, and (*c*) to include unloading or recovery process in the transient strain function.
(3) In the evaluation of transient material properties it is critically important to account for load-up strains to the constant stress condition of a creep test and to account for the strains induced during excavation of the salt samples, whether from deep drilling or coring from around underground rooms. There is a strong linear correlation between the free dislocation content and the calculated transient strain parameter of the MD constitutive equations. This relationship should be used to estimate the amount of prestrain contained in test specimens.

5.2 Importance of understanding transient behavior in excavations or under changing boundary conditions

In excavations such as those at the WIPP site, transient strain is important because the excavated room closures are the accumulation of the small transient strains throughout large volumes of material. For example, in a 600 day simulation at the WIPP of excavated room closure, the transient creep contribution was 1.2 times the steady-state contribution.

Another example of a situation in which transient behavior is important involves the thermal expansion induced in a borehole by a high-level nuclear waste cannister. If a waste package were to be emplaced in a borehole in a high-level nuclear waste repository in salt, stresses would build up in the waste package because of the thermal expansion of the surrounding salt and the waste package. Without heat, the maximum radial stress on the waste package that can be generated by the creeping salt is equal to the initial lateral stress that exists in the salt before any excavation. But, in very early times the salt will experience large temperature gradients around the waste package. High stresses will develop because the salt is constrained in all directions by the waste package and the surrounding cooler salt. As the temperature gradients diffuse out into the salt, the salt becomes less restrictive to deformation. The transient inelastic response of the salt is important in the early times because it has a major influence on the early magnitude and times of stress relaxation.

5.3 Strategic Petroleum Reserve (SPR)

In its capacity as science advisor to the DOE, Sandia has conducted extensive analyses of the creep behavior of various U.S. Gulf Coast salt domes as well as cavern closure behavior for the various sites that form the SPR. In the mid 1990's Sandia played a key role in analyzing the geomechanical response at Weeks Island. The Weeks Island SPR site is an underground mine, as opposed to most of the other SPR sites, which are leached caverns in salt. In the mid 90's, a large sinkhole formed above the surface of the mine, suggesting the possibility that the stored oil might not be contained in the mine, and break through to the surface. Sandia performed three-dimensional finite element analyses of the mine, and performed forward modeling to predict the future behavior of the mine in different scenarios (*Hoffman*, 1994). The Sandia analyses were pivotal in the ultimate decision to abandon the Weeks Island site, and back-fill the emptied mine with brine.

5.4 Assessment of the state of the art

Based on the validation studies at the WIPP site and on observations of SPR cavern behavior compared with model studies it can be concluded that the current state-of-the-art in salt modeling is adequate to model the deformations and stress fields of underground structural configurations for the ranges of temperature and stresses of interest to WIPP and SPR. Although the conditions expected for deepwater GoM field development are more severe than those encountered at the WIPP or SPR sites, they nonetheless fall within the ranges of stress and temperature for which the mechanistically based salt models have been developed. Thus, there should be no need for further fundamental salt model development. Moreover, without evidence to the contrary, the databases that exist for WIPP and SPR salts, could be used to allow scoping analyses specific to deepwater sub-salt and near-salt GoM field developments.

5.5 Expected salt behavior for near-salt and sub-salt deepwater GoM fields

Presented here are predicted steady-state strain rates for salt domes in deepwater GoM fields with a generic overburden profile. Data are determined for a nominal 4,000 ft water depth. The formations are normally pressured in which the smallest likely pore pressure has been assumed. Two relationships were used to compute the magnitude of the minimum horizontal stress. The first (most likely) is an empirical relationship used to compute minimum horizontal stresses in shales in the Gulf of Mexico. The second profile (worst case) is computed for sands having a lower Poisson's ratio than the shale, and so has a lower minimum stress. For both profiles, the stress difference used in the calculation of expected steady-state strain rates is the overburden stress minus the minimum horizontal stress. The temperature at the mudline was assumed 38 °F and assumed to increase at a rate of 1.45 °F per 100 feet of depth.

The steady-state strain rates that would exist in salt based on these two profiles were calculated using the Multimechanism Deformation Coupled Fracture (MDCF) model, that is detailed in Appendix E. As disscussed there, it is expected that at the depths of interest to deepwater GoM field developments, only the dislocation mechanisms will be active because of the very high mean stresses. Thus, brittle fracture mechanisms are assumed to be inactive. The specific deformation mechanisms for these conditions are presented in Appendix E and the material properties are given in Appendix F. The upper-bound, typical, and lower-bound values for steady-state strain rates were made using the steady-state properties of the Big Hill Salt Dome, WIPP salt, and Bryan Mound Dome, respectively. As shown in Appendix F, WIPP salt deformation behavior falls in the middle of the deformation behavior of the SPR dome salts and for this reason is termed "typical".

Tables 5.1 and 5.2 list the data and results for the two profiles, "most likely" (shale) and "worst case" (sand), respectively.

Table 5.1. Steady-state strain rates for the most likely (shale) stress profile.

Depth Feet	Depth below mudline Feet	Pore Pressure psi	Ovbd psi	Temp deg F	Fracture Gradient psi	Deviatoric Stress psi	Upper-Bound Steady-State Strain Rate, 1/s	Typical Steady-State Strain Rate, 1/s	Lower-Bound Steady-State Strain Rate, 1/s
4000	0	1766	1766	38	1766	0	0	0	0
4500	500	1987	2154	45	2045	109	2.07E-16	1.26E-16	3.79E-18
5000	1000	2208	2597	53	2341	256	1.99E-14	1.21E-14	3.64E-16
6000	2000	2649	3492	67	3140	352	1.56E-13	9.48E-14	2.85E-15
7000	3000	3091	4397	82	3948	449	8.45E-13	5.15E-13	1.55E-14
8000	4000	3532	5313	96	4766	547	3.47E-12	2.11E-12	6.34E-14
9000	5000	3974	6240	111	5594	646	1.23E-11	7.50E-12	2.25E-13
10000	6000	4416	7178	125	6431	746	3.73E-11	2.27E-11	6.82E-13
11000	7000	4857	8126	140	7279	848	1.05E-10	6.43E-11	1.93E-12
12000	8000	5299	9086	154	8135	951	2.69E-10	1.64E-10	4.92E-12
13000	9000	5740	10056	169	9002	1055	6.67E-10	4.07E-10	1.22E-11
14000	10000	6182	11038	183	9878	1160	1.55E-09	9.45E-10	2.83E-11
15000	11000	6623	12030	198	10763	1266	3.61E-09	2.20E-09	6.60E-11
16000	12000	7065	13033	212	11659	1374	8.09E-09	4.94E-09	1.48E-10
17000	13000	7506	14047	227	12564	1483	1.87E-08	1.14E-08	3.42E-10
18000	14000	7948	15072	241	13479	1593	4.21E-08	2.57E-08	7.71E-10
20000	16000	8831	17154	270	15337	1817	2.24E-07	1.37E-07	4.10E-09
22000	18000	9714	19280	299	17234	2046	1.18E-06	7.19E-07	2.16E-08
24000	20000	10597	21449	328	19170	2279	5.86E-06	3.57E-06	1.07E-07
26000	22000	11480	23662	357	21144	2518	2.69E-05	1.64E-05	4.91E-07
28000	24000	12363	25918	386	23157	2761	1.13E-04	6.88E-05	2.06E-06

Table 5.2. Steady-state strain rates for the worst case (sand) stress profile.

Depth Feet	Depth below mudline Feet	Pore Pressure psi	Ovbd psi	Temp deg F	Fracture Gradient psi	Deviatoric Stress psi	Upper-Bound Steady-State Strain Rate, 1/s	Typical Steady-State Strain Rate, 1/s	Lower-Bound Steady-State Strain Rate, 1/s
4000	0	1766	1766	38	1766	0	0		0
4500	500	1987	2154	45	1945	1900	5.42E-15	3.30E-15	9.91E-17
5000	1000	2208	2597	53	2338	2285	2.13E-14	1.30E-14	3.90E-16
6000	2000	2649	3492	67	2930	2863	1.61E-12	9.83E-13	2.95E-14
7000	3000	3091	4397	82	3526	3445	2.33E-11	1.42E-11	4.26E-13
8000	4000	3532	5313	96	4126	4030	1.68E-10	1.02E-10	3.07E-12
9000	5000	3974	6240	111	4729	4619	8.65E-10	5.27E-10	1.58E-11
10000	6000	4416	7178	125	5336	5211	3.44E-09	2.10E-09	6.30E-11
11000	7000	4857	8126	140	5947	5807	1.20E-08	7.33E-09	2.20E-10
12000	8000	5299	9086	154	6561	6407	3.66E-08	2.23E-08	6.70E-10
13000	9000	5740	10056	169	7179	7010	1.06E-07	6.47E-08	1.94E-09
14000	10000	6182	11038	183	7800	7617	3.20E-07	1.95E-07	5.86E-09
15000	11000	6623	12030	198	8425	8228	9.62E-07	5.87E-07	1.76E-08
16000	12000	7065	13033	212	9054	8842	2.87E-06	1.75E-06	5.24E-08
17000	13000	7506	14047	227	9687	9460	9.49E-06	5.78E-06	1.74E-07
18000	14000	7948	15072	241	10322	10081	3.38E-05	2.06E-05	6.19E-07
20000	16000	8831	17154	270	11605	11335	6.39E-04	3.90E-04	1.17E-05
22000	18000	9714	19280	299	12903	12604	1.75E-02	1.07E-02	3.21E-04
24000	20000	10597	21449	328	14214	13886	5.80E-01	3.53E-01	1.06E-02
26000	22000	11480	23662	357	15541	15184	2.09E+01	1.27E+01	3.82E-01
28000	24000	12363	25918	386	16882	16496	7.88E+02	4.81E+02	1.44E+01

Figures 5.1 and 5.2 show the steady-state strain rates as a function of depth on a semi-logarithmic scale for the most likely (shale) and worst case (sand) stress profiles, respectively. It should be noted that, as discussed in detail in Section 2, the strain rates calculated here are for the inelastic strains that salt would experience under the imposed temperatures and stress differences for unconstrained salt. The strain rates experienced in the field settings of interest may differ substantially.

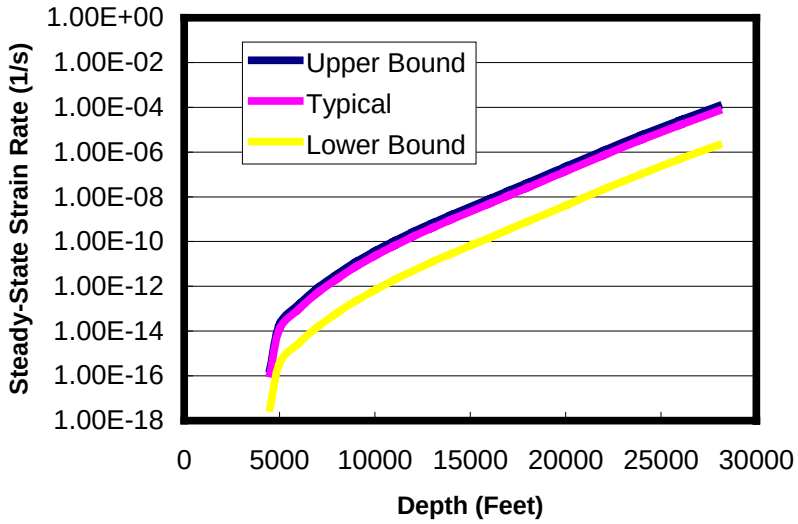

Figure 5.1. Range of steady-state strain rates versus depth for the most likely (shale) stress profile based on WIPP and SPR salts.

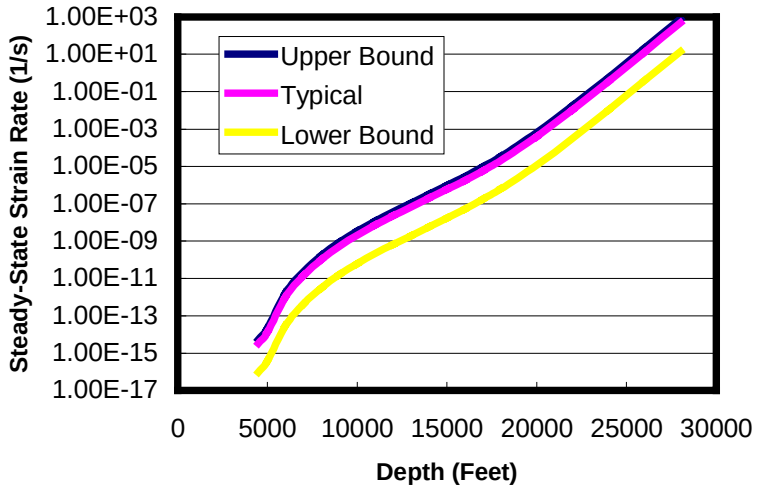

Figure 5.2. Range of steady-state strain rates versus depth for the worst case (sand) stress profile based on WIPP and SPR salts.

6 Appendix D – Correlation of Salt Strength and Deformation Properties with Chemical, Mineralogic, and Physical Characteristics of Salt

It is well known that the strength and deformation properties of salt are site dependent. There has been some evidence to suggest that such variability is caused by differences in salt chemistry, mineralogy, or other physical characteristics such as subgrain size, grain size distribution, or grain aspect ratio. For example, *Hansen et al*. (1987) demonstrated that increases in anhydrite content in salt reduce creep rates.

In 1995 the Solution Mining Research Institute (SMRI) commissioned RE/SPEC Inc. to compile a database of strength and deformation properties and chemical, mineralogic and physical characteristics of Gulf Coast dome salts from RE/SPEC's Sandia-funded and industry-funded characterization studies. The database was evaluated to determine correlations between strength and deformation properties and chemical, mineralogic, and physical characteristics of dome salt. The analyses are documented in *Pfeifle et al*. (1995) and summarized in the following sections.

6.1 Database

The database was assembled from test results obtained by RE/SPEC Inc. on salt recovered from 12 domes located in the Gulf Coast region of the United States. Testing was performed on specimens from multiple depths within the domes. The salt domes that were included in the study are listed in Table 6.1 together with the depth intervals, core recovery location, and whether the data are public or private.

Table 6.1. Gulf Coast domal salts used in correlation study.

Dome	Mine, Borehole or Well	Nominal Depth (ft)	Data Type
Avery Island, LA	Mine	500 700	Public
Barbers Hill, TX	SWD-4	1,400 1,450 1,500	Private
	Well #29	2,525 4,615	Private
	Well #3	2,255 3,715	Private
Cote Blanche, LA	Mine	1,350	Public
Jefferson Island, LA	Mine	1,500	Public
McIntosh, AL	BGS Well #1	4,075 4,650 5,210	Private
Napoleonville, LA	Well #19	2,185	Private
North Dayton, TX	LSC #1	Not Available	Private
Petal, MS	Well #6	2,550 4,185 4,705 5,335	Private

Richton, MS	MRIG-9	1,200	Public
Spindletop, TX	Sabine #1	4,065 4,605	Private
	Winnie #1	4,005	Private
Vacherie, LA	LSU #1	2,000	Public
Weeks Island, LA	Site H23	735	Public
	Site W14	735	Public

6.2 Strength and deformation properties

Properties were determined from 141 indirect tension tests, 294 unconfined and confined compression tests, and 139 creep tests performed at temperatures up to 473K. The properties included in the analyses were the following:

Strength
- Brazilian indirect tensile strength, T_0
- Unconfined compressive strength, C_0
- Angle of internal friction, ϕ
- Cohesion, C

Elastic Deformation
- Young's modulus, E
- Poisson's ratio, ν

Creep Deformation
- Steady-state creep rate, $\dot{\varepsilon}_s$
- Structure parameters, A^* and A'
- Stress-dependent exponent, n
- Activation energy parameter, Q

6.2.1 Brazilian indirect tension test

Tensile strength from the Brazilian indirect test is determined using the formula

$$T_0 = \frac{2P_f}{\pi DL} \tag{6.1}$$

where P_f is the line load at failure, and L and D are the length and diameter, respectively, of a right circular cylinder. The database includes 194 indirect tension tests on Gulf Coast dome salts performed at room temperature (20 °C). The specimens had a length-to-diameter (L:D) ratio of 0.5 and diameters of either 50 mm or 100mm. The test specimens were typically loaded in stroke control at a rate of 2.5 x 10^{-3} mm/s and produced failure in ≤ 10 minutes.

6.2.2 Compressive strength tests

The quasi-static compression test is conducted on right circular cylinders with an L:D ratio of 2. In the unconfined tests, the test specimen is loaded in the axial direction either in stress-rate or strain-rate control until failure occurs defined as the maximum stress in a stress-strain curve. In the confined tests, the specimen is first loaded hydrostatically to a prescribed level and then the axial load is increased either in stress-rate or strain-rate control until failure occurs. The test specimens in the RE/SPEC study were loaded in strain control at an axial strain rate of 1×10^{-4} s^{-1}, which produced failure in 5 to 15 minutes.

In the unconfined quasi-static compression tests, the measured strength is called the unconfined compressive strength, C_0, defined as the maximum or peak stress observed during the test. The strength is defined by a sharp peak in the stress-strain curve followed by a stress drop indicative of brittle failure. The database for this test included 239 unconfined compression tests performed at room temperature. The diameters of the test specimens were either 50 mm or 100 mm.

In the confined quasi-static compression tests, the strength is defined as the maximum stress difference observed in the test. Stress difference is defined as the difference between the applied axial stress and the confining pressure. For confining pressures less than about 5 MPa for salt, the strength is generally characterized by a sharp peak in the stress-strain curve indicative of brittle failure. For higher confining pressures, no distinct peak is observed. Rather, the applied load reaches a maximum value and the specimen continues to deform without a drop in axial stress. This type of failure is called ductile failure.

The strength of salt increases with confining pressure. To characterize this strength, a Mohr-Coulomb criterion is often used. To construct a Mohr-Coulomb criterion, each quasi-static compression test is plotted as a Mohr's circle. The envelope or line tangent to each of these circles defines the Mohr-Coulomb criterion and can be expressed as

$$\tau = C + \sigma \tan(\phi) \tag{6.2}$$

where τ and σ are the shear stress and normal stress, respectively; ϕ is the angle of internal friction; and C is the cohesion, i.e., the slope and intercept of the failure envelope respectively. Eq. (6.2) is valid for a limited range of normal stress. For higher values the failure envelope is nonlinear.

The database contains 55 confined quasi-static compression tests plus the 239 unconfined test results. The results were obtained at room temperature with right circular cylindrical specimens with a diameter of either 50 mm or 100 mm and L:D of 2.

6.2.3 Elastic moduli determination

Elastic moduli were determined from the first unload-reload cycle of the quasi-static compression test results. The elastic moduli are defined by

$$E = \frac{\Delta\sigma_1}{\Delta\varepsilon_1} \tag{6.3}$$

and

$$\nu = \frac{-\Delta\varepsilon_2 \bullet E}{\Delta\sigma_1} \tag{6.4}$$

where $\Delta\sigma_1$ is the increment in axial stress and $\Delta\varepsilon_1$ and $\Delta\varepsilon_2$ are the increments in the axial and radial strains, respectively. Eqs. (6.3-6.4) are valid only for the linear portion of the stress-strain curve called the elastic portion where deformations are fully recoverable upon unloading. For most rocks the initial loading part of the stress-strain curve represents elastic behavior and can be used to determine the elastic constants. For salt, however, the initial loading produces large inelastic strains in addition to the elastic strains. It is necessary, therefore, to perform one or more unload-reload cycles to minimize the inelastic components of strain and isolate the elastic components.

6.2.4 Confined triaxial compression creep tests

Salt exhibits time-dependent deformation when subjected to any level of shear stress. For this type of material the confined triaxial compression creep test is often performed. The test is usually conducted on a solid right circular cylinder of salt with an L:D of 2. The specimen is loaded hydrostatically to a prescribed pressure selected to simulate the overburden pressure in the salt at depth. Additional axial load is then applied rapidly to the specimen inducing an axial stress difference ($\sigma_1 - \sigma_3$). Specimen deformations are then measured with time while the confining pressure, stress difference, and temperature are held constant for the duration of the test.

Two or three creep stages comprise a typical creep curve for salt. Following the application of the stress difference, the deformation rate is very high. This rate then decreases monotonically with time until a constant rate of deformation is observed. These two stages are called transient and steady-state creep stages, respectively. For low enough confining pressure (< 5 MPa) a third stage becomes evident called the tertiary creep stage that is characterized by accelerating creep rates that cause dilation, an increase in volume through microfracturing, leading to failure.

In the correlation analyses, only the steady-state creep parameters were investigated with respect to the influence of chemical, mineralogic, and physical characteristics. As discussed previously, steady-state deformation of salt is controlled by micromechanical deformation mechanisms such a mass diffusion and the motion of dislocations within the crystal lattice of the salt. For the correlation analyses the Norton creep model was used to characterize the steady-state creep deformation of salt. This single-mechanism model is given by

$$\dot{\varepsilon}_s = A\Delta\sigma^n \exp\left(-\frac{Q}{RT}\right) \tag{6.5}$$

where $\dot{\varepsilon}_s$ is the steady-state creep rate, $\Delta\sigma$ is the stress difference, T is temperature, R is the universal gas constant, n is the stress component, Q is the activation energy, and A is a constant parameter typically determined from model fitting. This equation illustrates that the steady-state creep rate is strongly influenced by the magnitudes of both the stress difference and the temperature imposed in a creep test. The correlation analyses were performed for the steady-state strain rate, $\dot{\varepsilon}_s$, and three parameters, A, n, and Q. The database for these properties comprises nearly 200 creep tests performed on Gulf Coast dome salts at temperatures from 293 K to 473 K and stress differences from 2 MPa to 31 MPa. The diameters of the specimens were either 50 mm or 100 mm.

The most common method to estimate the steady-state creep rate is to fit a straight line to the linear portion of the strain-time curve. An assessment of the site-to-site variability in steady-state rates can be made when the test conditions are identical for a series of tests conducted on specimens recovered from different locations within a dome or among domes. Thus the database was searched to identify test conditions that were imposed in as large a number of tests as possible. Three such test conditions were identified for stress difference and temperature. These were (1) 20.69 MPa and 298 K, (2) 5 MPa and 373 K, and (3) 5 MPa and 473 K.

The exponent on stress in Eq. (6.5) is usually calculated by conducting a series of individual creep tests at different stress differences but identical temperatures. For constant temperature this equation is written as

$$\dot{\varepsilon}_s = A^*(\Delta\sigma)^n \tag{6.6}$$

where A^* is a model parameter that incorporates the effect of temperature, as well as the model parameter, A. A plot of steady-state strain rate versus stress difference in log space produces a straight line with slope n and intercept log (A^*).

The activation energy, Q, is usually calculated from creep tests performed at a constant stress difference but at different temperatures. These tests may be conducted on multiple specimens or on a single specimen in multiple stages in which the temperature is changed from one stage to the next. For constant stress difference tests, Eq. (7.5) can be rewritten as

$$\dot{\varepsilon}_s = A'\exp\left(-\frac{Q}{RT}\right) \tag{6.7}$$

where A' is a model parameter incorporating the stress dependency and the model parameter, A. Thus, a plot of the natural logarithm of the steady-state strain rate versus the reciprocal of the temperature produces a straight line with slope Q/R and intercept ln (A'). Q is readily determined, since R is a constant equal to 1.987 cal/mole K.

6.3 Chemical, mineralogic, and physical characteristics

The correlation study that included impure salts considered the following chemical, mineralogic, and physical characteristics:

Chemical
- Sodium, Na
- Chlorine, Cl
- Magnesium, Mg
- Potassium, K
- Calcium, Ca
- Sulfate, SO_4
- Water insolubles

Mineralogy
- Halite
- Anhydrite

Physical
- Grain size
- Grain size variability
- Grain aspect ratio
- Subgrain size

The chemical constituent database comprises 76 chemical analyses. The mineralogic constituent database comprises 52 analyses. The database for grain size, grain size variability, and grain aspect ratios comprises 33 samples, while that for subgrain size comprises 8 samples.

6.4 Correlation analysis

There were four major correlation classes. In the first class, strength and deformation properties were correlated with other strength and deformation properties. In the second class, strength and deformation properties were correlated with chemical constituents. In the third class, strength and deformation properties were correlated with mineralogic constituents. In the fourth class, strength and deformation properties were correlated with physical characteristics.

The correlations were quantified by a statistical parameter called the correlation coefficient. This coefficient is the ratio of the covariance of two variables and the product of their standard deviations. It ranges from –1 to +1. The extreme values, i.e., ± 1, indicate that the variables are highly correlated. A positive value means that higher than mean values of one variable are likely paired with higher than mean values of the other variable (or lower than mean values with lower than mean values). On the other hand a negative value means

that higher than mean values of one variable are likely paired with lower than mean values of the other variable.

6.5 Summary of correlation results

The results obtained from the correlation study are summarized in this section. These results may be useful in characterizing the salts encountered during development of sub-salt and near-salt deepwater GoM fields.

1. Subgrain size is a good indicator of strength and deformation properties for dome salt. For example, steady-state strain rate and the steady-state stress exponent are negatively correlated with subgrain size with correlation coefficients, ρ, of -0.87 and -0.92, respectively, as shown in Figure 6.1.
2. The steady-state strain rate determined at a temperature of 373K and a stress difference of 5 MPa is correlated with mean grain size ($\rho = 0.96$) and with grain aspect ratio ($\rho = 0.89$).
3. At 373K the steady-state stress exponent shows a strong, positive correlation with both sodium and chlorine (~0.90 based on four data pairs). Similar correlations for this exponent were found for halite (0.92 based on four data pairs) and anhydrite (-0.92 based on four data pairs).
4. The steady-state stress exponent shows strong correlations with sodium ($\rho = 0.9$), chlorine ($\rho = 0.9$), calcium ($\rho = -0.9$), and sulfate ($\rho = -0.9$).

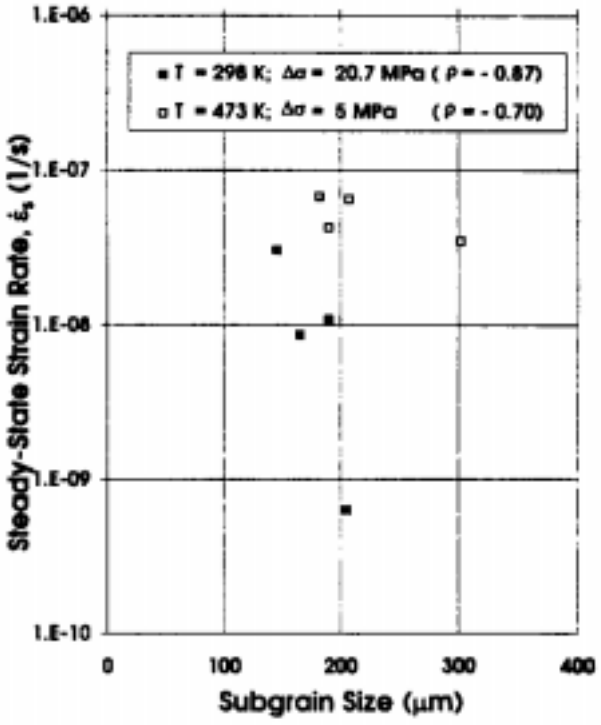

Figure 6.1. Correlation between steady-state creep rate and subgrain size (*Pfeifle et al.*, 1995).

5. The steady-state strain rate determined at a temperature of 298K and a stress difference of 20.69 MPa is correlated with magnesium ($\rho = 0.77$).
6. The angle of internal friction is correlated with potassium ($\rho = 0.7$) and with water insolubles ($\rho = 0.77$), while cohesion is negatively correlated with water insolubles ($\rho = -0.77$) .
7. Steady-state strain rates and the steady-state stress exponents are somewhat positively correlated with strength parameters while the thermal activation energy parameters are somewhat negatively correlated with strength parameters.
8. A negative correlation exists between cohesion and the angle of internal friction (-0.64 based on seven data pairs).
9. High positive correlation was found for: tensile strength and unconfined compressive strength (0.74 based on 23 data pairs); tensile strength and cohesion (0.66 based on seven data pairs); and unconfined compressive strength and cohesion (0.79 based on seven data pairs).

6.6 Discussion

Correlation analyses were used to determine the correlation of strength and deformation properties with chemical, mineralogic, and physical characteristics of Gulf Coast dome salts. The analyses used data from 12 Gulf Coast domes. It was found that the strongest correlations exist between the physical characteristics, in particular, subgrain size, and salt properties such as tensile and compressive strengths, steady-state strain rate, and steady-state stress exponent. Weaker, yet high, correlations were also found for the interdependence of strength and deformation properties with chemical, and mineralogic characteristics.

If the chemical, mineralogic, and physical characteristics of GoM salt domes could be determined, then it may be possible to obtain first estimates of the steady-state creep rates for these domes by using the linear dependency between the variables.

7 Appendix E – MDCF Constitutive Model for Salt

The constitutive model developed at Sandia for WIPP and SPR analyses is called the Multimechanism Deformation Coupled Fracture (MDCF) model. This model has been formulated by considering individual mechanisms that include dislocation creep, shear damage, tensile damage, and damage healing. The constitutive equations have been formulated on the basis that the total strain rate, $\dot{\varepsilon}_{ij}$, comprises an elastic term, $\dot{\varepsilon}^{e}_{ij}$, and an inelastic term, $\dot{\varepsilon}^{i}_{ij}$, according to

$$\dot{\varepsilon}_{ij} = \dot{\varepsilon}^{e}_{ij} + \dot{\varepsilon}^{i}_{ij} \tag{7.1}$$

in which the elastic strain rate is given by the generalized Hooke's law and the inelastic term is intended to treat all aspects of inelasticity. The generalized (3D) form of the inelastic strain rate is given by (*Fossum et al*., 1988)

$$\dot{\varepsilon}_{ij} = \frac{\partial \sigma^{\alpha}_{eq}}{\partial \sigma_{ij}} \dot{\varepsilon}^{\alpha}_{eq} \tag{7.2}$$

where σ^{α}_{eq} and $\dot{\varepsilon}^{\alpha}_{eq}$ are the power-conjugate equivalent stress and strain rate measures, respectively, for deformation mechanism α, with $\alpha = 1,2,3,\ldots n$, in a solid that exhibits n deformation mechanisms. This generalized flow law has been derived based on a thermodynamic formulation in which the power-conjugate equivalent stress measure plays the role of a flow potential and the derivative with respect to stress, σ_{ij}, defines the flow direction.

Inelastic flow in rock salt occurs by dislocation, microfracture, and damage healing mechanisms. The process driving forces for individual flow mechanisms are represented by appropriate power-conjugate equivalent stress measures, from which appropriate flow laws are derived and summed according to Eq. A.2. Thus, the overall flow law is (*Chan et al.*, 1992, 1994, 1995a)

$$\dot{\varepsilon}^{i}_{ij} = \frac{\partial \sigma^{c}_{eq}}{\partial \sigma_{ij}} \dot{\varepsilon}^{c}_{eq} + \frac{\partial \sigma^{\omega_s}_{eq}}{\partial \sigma_{ij}} \dot{\varepsilon}^{\omega_s}_{eq} + \frac{\partial \sigma^{\omega_t}_{eq}}{\partial \sigma_{ij}} \dot{\varepsilon}^{\omega_t}_{eq} + \frac{\partial \sigma^{h}_{eq}}{\partial \sigma_{ij}} \dot{\varepsilon}^{h}_{eq} \tag{7.3}$$

for coupled creep (c), shear damage (ω_s), tensile damage (ω_t), and damage healing (h). The superscripts to the equivalent strain rate, $\dot{\varepsilon}_{eq}$, and the power-conjugate stress measure, σ_{eq}, indicate quantities corresponding to individual mechanisms. A summary of the conjugate equivalent stress and strain rate measures for individual deformation mechanisms is presented next.

7.1 Conjugate equivalent stress measures

Inelastic flow caused by dislocation creep is volume preserving and independent of pressure. These features lead to a conjugate equivalent stress measure for dislocation creep, σ_{eq}^{c}, which is formulated based on the stress difference as given by *Munson et al*. (1990)

$$\sigma_{eq}^{c} = \left|\sigma_1 - \sigma_3\right| \tag{7.4}$$

where σ_1 and σ_3 are the maximum and minimum principal stresses, with compression being positive. This stress measure is preferred over that of von Mises because experimental measurements of the flow surface and inelastic strain rate vector are in better agreement with the former formulation (*Munson et al*., 1990).

Damage development in compression is considered to arise from sliding of microcracks by shear and the opening of wing-tip cleavage cracks that develop on some of the shear cracks. The resulting inelastic flow includes deviatoric and dilatational components with a pressure dependence. These characteristics have been accounted for in a nonassociated flow formulation by using two conjugate equivalent stress measures, one for the flow law and another for the kinetic equation. These stress measures are (*Chan et al*., 1992, 1994, 1996a)

$$\left[\sigma_{eq}^{\omega_s}\right]_f = \left|\sigma_1 - \sigma_3\right| - \frac{x_2 x_8}{3}\left[I_1 - \sigma_1\right] \tag{7.5}$$

for the flow law and

$$\left[\sigma_{eq}^{\omega_s}\right]_k = \left|\sigma_1 - \sigma_3\right| - x_2 x_7 \,\mathrm{sgn}(I_1 - \sigma_1)\left[\frac{I_1 - \sigma_1}{3x_7 \,\mathrm{sgn}(I_1 - \sigma_1)}\right]^{x_6} \tag{7.6}$$

for the kinetic equation; where I_1 is the first invariant of Cauchy stress; the x_i's are material constants; and sgn( ) is the signum function. The first terms on the RHS of Eqs. (7.5) and (7.6) represent shear-induced damage, which manifests as slip-induced shear microcracks. Some of these microcracks develop wing tips that generate irreversible inelastic strains that add to those originating from dislocation flow mechanisms. Opening of these wing cracks, which are aligned parallel to the maximum principal stress (σ_1), occurs in directions normal to the σ_1 direction and is resisted by compressive stresses of σ_2 and σ_3. The second terms in the RHS of Eqs. (7.5) and (7.6), which are in the form of $f(I_1 - \sigma_1)$, model the effects of stress state on aiding or suppressing the opening of wing cracks.

Tensile creep damage in salt occurs in the form of cleavage microcracks aligned normal to the tensile stress. The kinetics of tensile damage in salt is substantially faster than shear damage and is therefore treated as a separate term. The conjugate equivalent stress measure for tensile damage-induced flow is (*Chan et al*., 1996a)

$$\sigma_{eq}^{\omega_t} = -x_1 \sigma_3 H(-\sigma_3) \tag{7.7}$$

where H( ) denotes the Heaviside step function. This stress measure is intended to represent the opening of microcracks by a tensile stress, σ_3.

Reduction of damage in rock salt can occur by the closure of open microcracks and the sintering of microcracks. Both of these processes can be considered to be driven by an identical thermodynamic driving force represented by a pertinent power-conjugate equivalent stress measure. If the healing process is isotropic, the appropriate power-conjugate equivalent stress measure is the first invariant, I_1, of the Cauchy stress. On the other hand, damage healing might be nonisotropic or exhibit induced anisotropy. For this situation, a second stress term in addition to I_1 is required. For describing stress-induced healing anisotropy, the conjugate equivalent stress measure for damage healing may be taken as (*Chan et al.*, 1995a)

$$\sigma_{eq}^{h} = \frac{1}{3}\left(I_1 - x_{10}\sigma_1\right) \tag{7.7}$$

where x_{10} is a material constant. One of the characteristics of this conjugate equivalent stress measure is that when used in conjunction with Eq. (7.3), the healing term is the only nonzero term under hydrostatic compression. But, in addition, healing may also occur under nonhydrostatic compression.

7.2 Equivalent strain-rate measures

The kinetic equation representing the creep rate, $\dot{\varepsilon}_{eq}^{c}$, caused by dislocation flow mechanisms was formulated by *Munson and Dawson* (1984) and is given by

$$\dot{\varepsilon}_{eq}^{c} = F \sum_{i=1}^{3} \dot{\varepsilon}_{s_i} \tag{7.8}$$

where F is a function representing transient creep behavior, $\dot{\varepsilon}_{s_i}$ is the steady state strain rate for the ith independent dislocation flow mechanism. The mechanisms include dislocation climb (i = 1), dislocation glide (i = 3), and one that has not been identified mechanistically but which is fully characterized experimentally (i = 2). The steady state strain rates are

$$\dot{\varepsilon}_{s_i} = A_i e^{-Q_i/RT} \left[\frac{\sigma_{eq}^{c}}{G(1-\omega)} \right]^{n_i} \tag{7.9}$$

for i = 1, and 2, and

$$\dot{\varepsilon}_{s_i} = H\left(\sum_{i=1}^{2} B_i e^{-Q_i/RT}\right)\sinh\left[\frac{q}{G}\left(\frac{\sigma_{eq}^{c}}{1-\omega} - \sigma_0\right)\right] \tag{7.10}$$

for i = 3; where the A_i's and B_i's are constants; Q_i's are activation energies; T is absolute temperature; R is the universal gas constant; G is shear modulus; n_i's are the stress exponents; q is the stress constant; H is the Heaviside function with $[\sigma_{eq}^{c}/(1-\omega) - \sigma_0]$ as the argument; and σ_0 is the stress limit of the dislocation glide mechanism.

The transient function, F, is given by

$$F = \begin{cases} \exp\left[\Delta\left(1 - \dfrac{\zeta}{\varepsilon_t^*}\right)^2\right], & \zeta \le \varepsilon_t^* \\ 1, & \zeta = \varepsilon_t^* \\ \exp\left[-\delta\left(1 - \dfrac{\zeta}{\varepsilon_t^*}\right)^2\right], & \zeta \ge \varepsilon_t^* \end{cases} \tag{7.11}$$

which comprises a work-hardening branch, an equilibrium branch, and a recovery branch. In Eq. (7.11), Δ and δ represent the work-hardening and recovery parameters, respectively, and both may be stress dependent; ζ is the hardening variable; and ε_t^* is the transient strain limit. The temperature and stress dependence of the transient strain limit is represented by (*Chan et al.*, 1994)

$$\varepsilon_t^* = K_0 e^{cT}\left(\frac{\sigma_{eq}^{c}}{G(1-\omega)}\right)^m \tag{7.12}$$

where K_0, c, and m are constants. The evolution rate, $\dot{\zeta}$, of the isotropic hardening variable ζ is governed by

$$\dot{\zeta} = (F-1)\dot{\varepsilon}_s \tag{7.13}$$

which approaches zero when the steady-state condition is achieved.

The kinetic equation of damage-induced inelastic flow was developed on the basis that wing cracks initiated at the tips of sliding shear cracks or slipbands. As a result, the kinetic equation for shear-induced damage followed closely to that for dislocation glide. The same form of expression was also used for the kinetic equation for tensile damage-induced flow law is given by (*Chan et al.*, 1994, 1996a)

$$\dot{\varepsilon}_{eq}^{\omega_i} = F^{\omega_i}\dot{\varepsilon}_s^{\omega_i} \tag{7.14}$$

where $i = s$ or t for shear or tensile damage, respectively; F^{ω_i} are the transient functions for the i^{th} mode of damage given by

$$F^{\omega_t} = F \exp\left(\frac{c_4\left(\sigma_{eq}^{\omega_t} - c_5\right)}{\sigma_0} \right) \tag{7.15}$$

$$F^{\omega_s} = F \exp\left(\frac{c_4\left(\sigma_{eq}^{c} - c_5\right)}{\sigma_0} \right) \tag{7.16}$$

The kinetic equations for damage-induced flow, $\dot{\varepsilon}_s^{\omega_t}$, during steady-state creep are expressed by

$$\dot{\varepsilon}_s^{\omega_t} = c_0\left(\sum_{i=1}^{2} B_i e^{-Q_i/RT} \right) \omega_0 e^{c_3\omega} \left[\sinh\left(\frac{c_2 \sigma_{eq}^{\omega_i} H\left(\sigma_{eq}^{\omega_i}\right)}{(1-\omega)G} \right)^{n_3} \right] \tag{7.17}$$

where the c_i's and n_3 are material constants and ω_0 is the initial value of the damage variable, ω. The kinetic equations in Eq. (7.17) allow $\dot{\varepsilon}_{eq}^{\omega_i}$ to exhibit a transient behavior by virtue of the transient function, F^{ω_i}, which is directly related to the transient function, F, for creep.

Experimental evidence indicates that two healing mechanisms may be present in WIPP salt. Each of the two healing mechanisms may be described by a first-order kinetic equation. The first mechanism, which is closure of microcracks, has a smaller time constant, τ_1, than the time constant, τ_2, for the second mechanism, which is healing of microcracks. The kinetic equation for damage healing in WIPP salt is taken to be (*Chan et al*. 1996b)

$$\dot{\varepsilon}_{eq}^{h} = \frac{\varepsilon_{kk}\left(\sigma_{eq}^{h} - \sigma_b\right) H\left(\sigma_{eq}^{h} - \sigma_b\right)}{\tau G} \tag{7.18}$$

with

$$\sigma_b = x_7 \left| \frac{\sigma_1 - \sigma_3}{x_2 x_7} \right|^{\frac{1}{x_6}} \tag{7.19}$$

where ε_{kk} is the volumetric strain, and τ is the characteristic time for damage healing. In general, damage healing tends to reduce ε_{kk} to zero. To account for two characteristic times, τ, is taken to be a function of the volumetric strain such that the characteristic time τ, approaches τ_1, when the volumetric strain becomes large but approaches τ_2 when the reverse is true.

7.3 Damage evolution equations

An internal variable in the context of Kachanov's isotropic damage parameter, ω, is used as a measure of current damage in the deformed salt. Damage development in the MDCF model is described in terms of an evolution equation that contains both damage growth and healing terms, as given by (*Chan et al*., 1995a)

$$\dot{\omega} = g(\omega, T, \sigma_{eq}^{\omega_i}, \chi_i) - h\left(\omega, T, \sigma_{eq}^{h}\right) \tag{7.20}$$

where $g(\omega, T, \sigma_{eq}^{\omega_i}, \chi_i)$ describes the growth of damage, and $h\left(\omega, T, \sigma_{eq}^{h}\right)$ describes the healing of damage. The damage growth function, *g*, is given by (*Chan et al*., 1994, 1996a)

$$g = \frac{x_4}{t_0}\omega\left[\ln\left(\frac{1}{\omega}\right)\right]^{\frac{x_4+1}{x_4}}\left\{\left[\frac{\sigma_{eq}^{\omega_s} H\left(\sigma_{eq}^{\omega_s}\right)}{\chi_s}\right]^{x_{3s}} + \left[\frac{\sigma_{eq}^{\omega_t} H\left(\sigma_{eq}^{\omega_t}\right)}{\chi_t}\right]^{x_{3t}}\right\} \tag{7.21}$$

where x_{3i}, x_4, χ_i (with $i = s$ or t for shear or tensile damage, respectively) are material constants, and t_0 is a reference time. The healing function is taken to be a first-order kinetic equation given by

$$h = \frac{\omega\left(\sigma_{eq}^{h} - \sigma_b\right)H\left(\sigma_{eq}^{h} - \sigma_b\right)}{\tau G} \tag{7.22}$$

which as the same form as the kinetic equation for damage healing.

7.4 Summary

The MDCF model has been formulated based on the unified constitutive approach in which both plasticity and creep are treated using the same set of flow laws, kinetic equations, and evolution equations of the internal variables. Consequently, plastic flow can be modeled without the use of yield and loading/unloading criteria.

The utility of the MDCF model has been demonstrated for creep, quasi-static compression, and for healing conditions. The model has been used in conjunction with a finite element code for predicting the failure of underground structures at the WIPP and in SPR studies. Coupling of creep and damage in the MDCF model allows calculation of the entire creep curves, including tertiary creep.

While the MDCF model is very general and can accommodate a wide range of deformation behavior, it is doubtful that more than the dislocation deformation mechanisms will be required in structural analyses for the conditions expected for deepwater GoM field developments, i.e., very high mean stresses.

8 Appendix F – Constitutive Parameters for WIPP and Gulf Coast Domal Salts

Here, the material constants for the MDCF model as discussed in Appendix E, are presented for WIPP salt and several Gulf Coast dome salts. The fracture constants have not been determined for the Gulf Coast salt domes. It is doubtful that the fracture constants will be needed because of the very high mean stresses that will be present at the depths of interest to sub-salt deepwater GoM field developments.

8.1 WIPP salt

The material constants presented here are those in current use for thermal/structural calculations in the WIPP Project. The parameters are for the MDCF model, which, in the absence of fracture, reduces to the Multimechanism Deformation (MD) model.

Table 8.1. MDCF creep and fracture constants for WIPP salt.

Creep			Fracture	
Parameter	Value		Parameter	Value
G, GPa	12.4		x_1	6
E, GPa	31.0		x_2	9
A_1, s^{-1}	8.386 E22		x_{3s}	5.5
Q_1, Kcal/mol	25		x_{3t}	40
N_1	5.5		x_4	3
B_1, s^{-1}	6.086 E6		$\chi_s\ (\sigma > \sigma_0)$, MPa	231.0
A_2, s^{-1}	9.672 E12		$\chi_s\ (\sigma \le \sigma_0)$, MPa	351.1
Q_2, Kcal/mol	10		χ_t, Mpa	15.15
N_2	5.0		x_6	0.75
B_2, s^{-1}	3.034E-2		x_7, MPa	1.0
σ_0 , MPa	20.57		x_8	0.1
Q	5.335 E3		c_0	5 E4
R, cal/mol-deg	1.987		c_2	850
M	3		c_3	10
K_0	6.275 E5		c_4	6
C, T^{-1}	9.198 E-3		c_5, MPa	25
α_w	-17.37		t_0, s	1
β_w	-7.738		n_3	3
δ	0.58		ω_0	≥ 1 E-4

8.2 Gulf Coast salt domes

The creep parameters in Table8.2 are from *Munson* (1999). Figures 8.1 and 8.2 illustrate the variability that exists among the different salts.

Table 8.2. MD creep parameters for Gulf Coast salt domes.

Creep Parameter	Avery Island	Weeks Island	Bryan Mound	West Hackberry	Big Hill	Bayou Choctaw	Moss Bluff	Jennings
G, GPa	12.4	12.4	12.4	12.4	12.4	12.4	12.4	12.4
E, GPa	31.0	31.0	31.0	31.0	31.0	31.0	31.0	31.0
A_1, s^{-1}	5.954E22	4.948E22	0.2516E22	9.812E22	13.75E22	1.929E22	5.870E22	1.090E22
Q_1, Kcal/mol	25	25	25	25	25	25	25	25
n_1	5.5	5.5	5.5	5.5	5.5	5.5	5.5	5.5
B_1, s^{-1}	4.321E6	3.591E6	0.1826E6	7.121E6	9.981E6	1.400E6	4.260E6	0.7912E6
A_2, s^{-1}	6.869E12	5.706E12	0.2609E12	11.32E12	15.85E12	2.250E12	6.770E12	1.222E12
Q_2, Kcal/mol	10	10	10	10	10	10	10	10
n_2	5.0	5.0	5.0	5.0	5.0	5.0	5.0	5.0
B_2, s^{-1}	2.154E-2	1.790E-2	0.0910E-2	3.550E-2	4.976E-2	6.978E-3	2.124E-2	0.3944E-2
σ_0 , MPa	20.57	20.57	20.57	20.57	20.57	20.57	20.57	20.57
q	5.335E3	5.335E3	5.335E3	5.335E3	5.335E3	5.335E3	5.335E3	5.335E3
R, cal/mol-deg	1.987	1.987	1.987	1.987	1.987	1.987	1.987	1.987
m	3	3	3	3	3	3	3	3
K_0	1.342E5	6.275E5	1.335E5	9.777E5	8.512E5	6.275E5	8.964E5	1.308E5
c, T^{-1}	9.198E-3	9.198E-3	9.198E-3	9.198E-3	9.198E-3	9.198E-3	9.198E-3	9.198E-3
α_w	-13.20	-17.35	-13.37	-17.37	-13.73	-13.73	-13.73	-13.73
β_w	-7.738	-7.738	-7.738	-7.738	-7.738	-7.738	-7.738	-7.738
δ	0.58	0.58	0.58	0.58	0.58	0.58	0.58	0.58

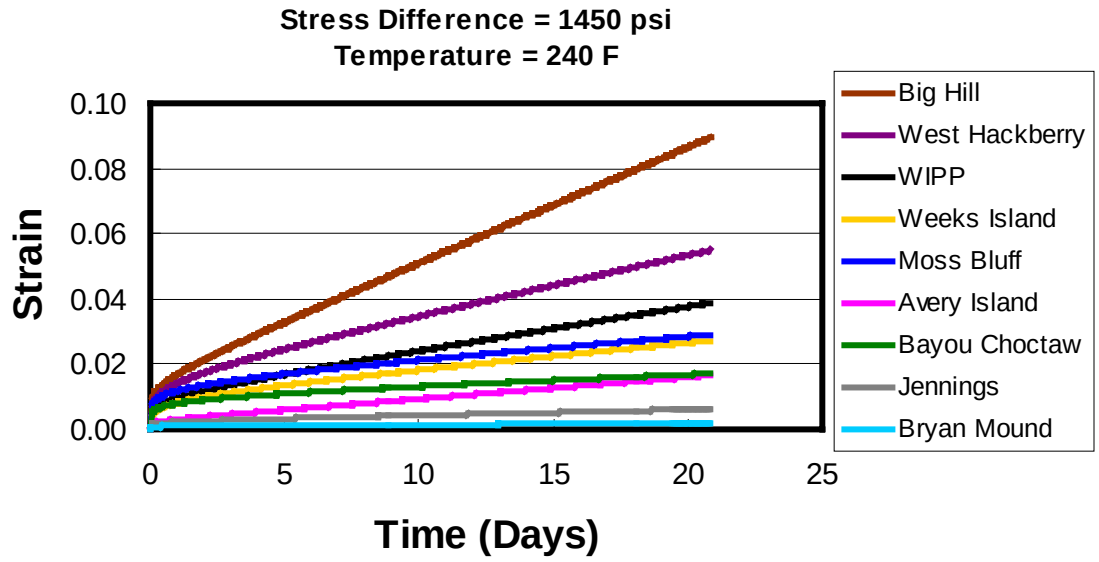

Figure 8.1. Comparison of creep behavior to 21 days for WIPP and Gulf Coast domal salts.

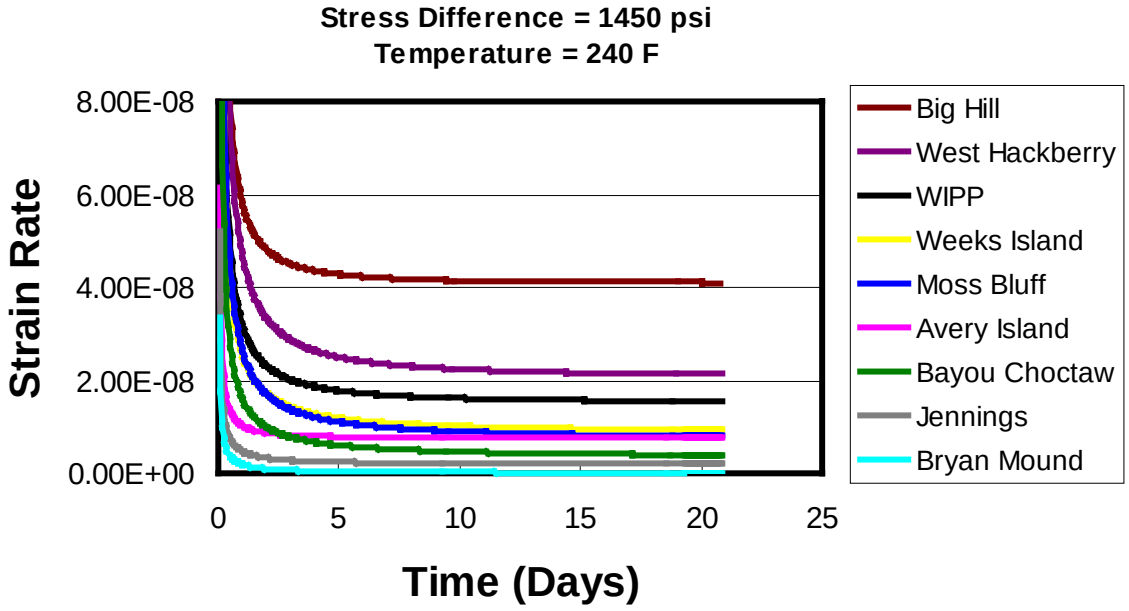

Figure 8.2. Comparison of strain rate behavior to 21 days for WIPP and Gulf Coast domal salts.

References

Arieli, A., H.C. Heard, and A.K. Mukherjee, "Deformation Modeling in Sodium Chloride at Intermediate and Elevated Temperatures," in *Mechanical Testing for Deformation Model Development* (Edited by R.W. Rohde and J.C. Swearengen), ASTM STP 765, pp. 342-365, American Society for Testing and Materials, Val Harvour, FL, 1982.

Bevan, T., T. Heyn, and P. Vinson, "Sub-Salt Drilling Project: Geoscience Perspective for Enhanced Drilling through Salt in the Gulf of Mexico," BP Amoco Report No. HO99.0010 February 1999.

Brodsky, N.S., and D.E. Munson, "The Effect of Brine on the Creep of WIPP Salt in Laboratory Tests," *Proc. 32nd U.S. Symp. on Rock Mech.*, University of Oklahoma, Norman, pp. 703-712, 1991.

Carter, N.L., and F.D. Hansen, "Creep of Rocksalt," *Tectonophysics*, Vol. 92, pp. 275-333, 1983.

Carter, N.L., F.D. Hansen, and P.E. Senseny, "Stress Magnitudes in Natural Rock Salt," *J. Geophys. Res.* Vol. 87, pp. 9289-9300, 1982.

Chan, K.S., N.S. Brodsky, A.F. Fossum, S.R. Bodner, and D.E. Munson, "Damage-Induced Nonassociated Inelastic Flow in Rock Salt," *Int. J. of Plasticity*, pp. 623-642, 1994.

Chan, K.S., D.E. Munson, S.R. Bodner, and A.F. Fossum, "Cleavage and Creep Fracture of Rock Salt," *Acta Mater*. Vol. 44, pp. 3553-3565, 1996.

Dorn, J.E., "The Spectrum of Activation Energies for Creep," *A Seminar on Creep and Recovery of Metals*, pp. 255-283, American Society for Metals, Cleveland, OH, 1956.

Durham, W.B., H.C. Heard, C.O. Boro, K.T. Keller, W.E. Ralph, and D.A. Trimmer, "Thermal Properties of Permian Basin Evaporites to 493 K Temperature and 30 MPa Confining Pressure," Report BMI/ONWI-633, Prepared by Lawrence Livermore National Laboratory, CA, for Office of Nuclear Waste Isolation, Battelle Memorial Institute, Columbus, OH, 1987.

Fossum, A.F., N.S. Brodsky, K.S. Chan, and D.E. Munson, "Experimental Evaluation of a Constitutive Model for Inelastic Flow and Damage Evolution in Solids Subjected to Triaxial Compression," *Int. J. Rock Mech. Min Sci & Geomech. Abstr.* Vol. 30, pp. 1341-1344, 1993.

Frost, H.J. and M.F. Ashby, *Deformation Mechanism Maps*, Pergamon Press, New York, 1982.

Guillope, M. and J.P. Poirier,"Dynamic Recrystallization during Creep of Single-Crystalline Halite: an Experimental Study," *J. Geophys. Res.* Vol. 84, pp. 5557-5567, 1979.

Hansen, F.D., and K.D. Mellegard, "Quasi-Static Strength and Deformational Characteristics of Domal Salt from Avery Island, Louisiana," Report ONWI-116. Prepared by RE/SPEC Inc. for Office of Nuclear Waste Isolation, Battelle Memorial Institute, Columbus, OH, 1980.

Hansen, F.D., K.D. Mellegard, and P.E. Senseny, "Elasticity and Strength of Ten Natural Rock Salts," *First Conf. on the Mechanical Behavior of Salt*, University Park, PA, 1981, pp. 71-83, 1984.

Hansen, F.D., P.E. Senseny, T.W. Pfeifle, and T.J. Vogt, "Influence of Impurities on Creep of Salt from the Palo Duro Basin," *Proc. 29th U.S. Symp. on Rock Mech.*, University of Minnesota, Minneapolis, MN. P.A. Cundall, R.L. Sterling, and A.M. Starfield (eds.), A. A. Balkema, Rotterdam, pp. 199-206, 1987.

Hunsche, U.E., in *7th Symp. on Salt,* Vol. 1, H. Kakihana, et al. (eds), Elsevier Science Publication, New York, NY, pp. 59-65, 1993.

Joffe, V.A., M.W. Kirpitschewa, and M.A. Lewitzky, "Deformation und Festigkeit der Kristalle," *Z. Phys.* Vol. 22, pp. 286-302, 1924.

Hoffman, E. L., "Stability Evaluation of the Markel Mine at Weeks Island, Louisiana," SAND93-4031, Sandia National Laboratories, Albuquerque, NM, 1994.

Krieg, R.D., "Reference Stratigraphy and Rock Properties for the Waste Isolation Pilot Plant (WIPP) Project," SAND83-1908, Sandia National Laboratories, Albuquerque, NM, 1984.

Mellegard, K.D., G.D. Callahan, and P.E. Senseny, "Multiaxial Creep of Natural Rock Salt," SAND91-7083, Sandia National Laboratories, Albuquerque, NM, pp. 1-60, 1992.

Morgan, H.S., C.M. Stone, and R.D. Krieg, "Evaluation of WIPP Structural Modeling Capabilities Based on Comparisons with South Drift Data," SAND85-0323, Sandia National Laboratories, Albuquerque, NM, 1986.

Munson, D.E., "Preliminary Deformation-Mechanism Map for Salt (with Application to WIPP)," SAND79-0076, Sandia National Laboratories, Albuquerque, NM, 1979.

Munson, D.E., and P.R. Dawson, "Constitutive Model for the Low Temperature Creep of Salt (with Application to WIPP)," SAND79-1853, Sandia National Laboratories, Albuquerque, NM, 1979.

Munson, D.E., and A.F. Fossum, "Comparison between Predicted and Measured South Drift Closures at the WIPP using a Transient Creep Model for Salt," *Proc. 27th U.S. Symposium on Rock Mechanics*, Tuscaloosa, AL, June 23-25, 1986.

Munson, D.E., A.F. Fossum, and P.E. Senseny, "Approach to First Principles Model Prediction of Measured WIPP (Waste Isolation Pilot Plant) In-Situ Room Closure in Salt," *Tunneling and Underground Space Technology*, Vol. 5, pp 135-139, 1990.

Pfeifle, T.W., K.D. Mellegard, and P.E. Senseny, "Preliminary Constitutive Properties for Salt and Nonsalt Rocks from Four Potential Repository Sites," Report ONWI-450, prepared by RE/SPEC Inc. for Office of Nuclear Waste Isolation, Battelle Memorial Institute, Columbus, OH, 1983.

Pfeifle, T.W., T.J. Vogt, and G.A. Brekken, "Correlation of Chemical, Mineralogic, and Physical Characteristics of Gulf Coast Dome Salt to Deformation and Strength Properties," *SMRI 1996 Spring Meeting, Houston, TX,* 1995.

Skrotzki, W., and Z.G. Liu, "Analysis of Cross Slip Process in Alkali Halides," *Physica Stat. Sol.* Vol. 8, p. 161, 1982.

Skrotzki, W., and P. Haasen "Plastic Deformation and Hardening of Polycrystalline Halides," *Int. Symp on Plastic Deformation of Ceramic Materials,* State College, PA, pp. 1-16, 1983.

Spiers, C.J., J.L. Urai, C.J. Peach, and H.J. Zwart, "The Effect of Brine (Inherent and Added) on Rheology and Deformation Mechanisms in Salt Rock," *2nd Conf. on the Mechanical Behavior of Salt,* Hannover,Germany, 1984, pp. 89-102, 1988.

Spiers, C.J., J.L. Urai, G.S. Lister, J.N. Boland, and H.J. Zwart, "Influence of Fluid-Rock Interaction on the Rheology of Salt Rock," Report EUR-10399, Commission of the European Comunities, Luxembourg, 1986.

Senseny, P.E. "Triaxial Compression Creep Tests on Salt from the Waste Isolation Pilot Plant," SAND85-7261, Sandia National Laboratories, Albuquerque, NM, 1986.

Senseny, P.E., and A.F. Fossum, "On Testing Requirements for Viscoplastic Constitutive Parameter Estimation," *J. of Engineering Materials and Technology*, Vol. 117, pp. 151-156, 1995.

Senseny, P.E., F.D. Hansen, J.E. Russell, N.L. Carter, and J.W. Handin, "Mechanical Behavior of Rock Salt: Phenomenology and Micromechanisms," *Int. J. Rock Mech. Min Sci & Geomech. Abstr.* Vol. 29, No 4, pp. 363-378, 1992.

Van Sambeek, L., A. Fossum, G. Callahan, and J. Ratigan, "Salt Mechanics: Empirical and Theoretical Developments," *7th Symposium on Salt*, Vol. I, pp. 127-134, 1993.

Varo, L., and E. K. S. Passaris, "The Role of Water on the Creep Properties of Halite," *Conf. on Rock Engineering*, University of Newcastle upon Tyne, United Kingdom, pp. 85-100, 1977.

von Mises, R, "Mechanik der Plastischen Formanderung von Kristallen," *Z. Angew. Mech.* Vol. 8, p. 161, 1928.

Wawersik, W.R, and D.W. Hannum, "Interim Summary of Sandia Creep Experiments on Rock Salt from the WIPP Study Area, Southeastern NM," SAND79-0115, Sandia National Laboratories, Albuquerque, NM, 1979.

Yang, J.M., Thermophysical Properties. In *Physical Properties Data for Rock Salt* (Edited by L.H. Gevantman), *Natioal Bureau of Standards Monograph 167*, pp. 205-221. U.S. Government Printing Office, Washington, DC, 1981.

External Distribution:

BP Corporation (3)
501 WestLake Park Blvd.
Houston, TX 77079-2696
Steve Willson (2)
Phil Patillo (1)

Conoco, Inc. (3)
Giin-Fa Fuh (2)
P.O. Box 2197
Houston, TX 77252-2197

Ernie Onyia (1)
400 E. Kaliste Saloom Road (70508)
P.O. Box 51266
Lafayette, LA 70505

Exxon Mobil (3)
3120 Buffalo Speedway
P.O. Box 2189
Houston, TX 77252-2189
Dave Olgaard
Steinar Ottesen
David Yale

Kerr McGee (3)
16666 Northchase
Houston, TX 77060
Mike Davis

Halliburton Technology Center (3)
2600 S. 2nd Street
P.O. Box 1431
Duncan, OK 73536-0426
Wolfgang Deeg

Phillips Petroleum Company (3)
140 Geoscience Building
Bartlesville, OK 74004
Lee Chin
Neal Nagel
Carl Montgomery

BHP Billiton Petroleum (Americas) Inc. (3)
1360 Post Oak Blvd. Suite 150

Houston, TX 77056
Jim McFadden (3)

ChevronTexaco Exploration and Production Technology Co. (3)
2202 Oil Center Court
Houston, TX 77073
Harvey Goodman (2)
Peng Ray (1)

Internal Distribution:

MS0750 J. T. Fredrich, 6116 (5)
MS0750 D. F. Aldridge
MS0750 D. J. Borns
MS0750 D. Coblentz, 6116
MS0750 N. R. Warpinski, 6116
MS0750 B. J. Thorne, 6116
MS0750 M.C. Walck, 6116
MS0751 A. F. Fossum, 6117 (5)
MS0751 L. S. Costin, 6117
MS0706 D. E. Munson, 6113
MS0706 T. E. Hinkebein, 6113
MS0701 R. E. Finley, 6100
MS9018 Central Technical Files, 8945-1
MS0899 Technical Library, 9616 (2)
MS0612 Review and Approval Desk, 9612
for DOE/OSTI